Upstream flow effects revealed in the EastGRIP ice core using a Monte Carlo inversion of a two-dimensional ice-flow model

Tamara Annina Gerber[1], Christine Schøtt Hvidberg[1], Sune Olander Rasmussen[1], Steven Franke[2], Giulia Sinnl[1], Aslak Grinsted[1], Daniela Jansen[2], and Dorthe Dahl-Jensen[1, 3]

[1]Section for the Physics of Ice, Climate and Earth, The Niels Bohr Institute, University of Copenhagen, Copenhagen, Denmark
[2]Alfred Wegener Institute, Helmholtz Centre for Polar and Marine Research, Bremerhaven, Germany
[3]Centre for Earth Observation Science, University of Manitoba, Winnipeg, Canada

Correspondence: Tamara Annina Gerber (tamara.gerber@nbi.ku.dk)

Abstract. The Northeast Greenland Ice Stream (NEGIS) is the largest active ice stream on the Greenland Ice Sheet (GrIS) and a crucial contributor to the ice-sheet mass balance. To investigate the ice-stream dynamics and to gain information about the past climate, a deep ice core is drilled in the upstream part of the NEGIS, termed the East Greenland Ice-Core Project (EastGRIP). Upstream flow effects introduce non-climatic bias in ice cores and are particularly strong at EastGRIP due to high ice-flow velocities and the location inside an ice stream on the eastern flank of the GrIS. Understanding and ultimately correcting for such effects requires information on the source area and the local atmospheric conditions at the time of ice deposition. We use a two-dimensional Dansgaard–Johnsen model to simulate ice flow along three approximated flow lines between the summit of the ice sheet (GRIP) and EastGRIP. Model parameters are determined using a Monte Carlo inversion by minimizing the misfit between modelled isochrones and isochrones observed in radio-echo-sounding (RES) images. We calculate backward-in-time particle trajectories to determine the source area of ice found in the EastGRIP ice core and present estimates of surface elevation and past accumulation rates at the deposition site. Our results indicate that increased accumulation in the upstream area is predominantly responsible for the constant annual layer thicknesses observed in the upper part of the ice column at EastGRIP. Inverted model parameters suggest that the imprint of basal melting and sliding is present in large segments along the flow profiles and that most internal ice deformation happens in the lower half of the ice column. The results of this study act as a basis for applying upstream corrections to a variety of ice-core measurements, and the model parameters are useful constraints for more sophisticated modelling approaches in the future.

1 Introduction

The East Greenland Ice-Core Project (EastGRIP) is the first attempt to retrieve a deep ice core inside an active ice stream. The drill site is located in the upstream part of the Northeast Greenland Ice Stream (NEGIS, Fahnestock et al., 1993), which

is a substantial contributor to the Greenland Ice Sheet (GrIS) mass balance (Khan et al., 2014) and accounts for around 12 % of its total ice discharge (Rignot and Mouginot, 2012). Understanding the driving mechanisms of the NEGIS is essential to anticipate its future development and potential impact on the ice-sheet stability with large-scale ice-flow models (Joughin et al., 2001; Khan et al., 2014; Vallelonga et al., 2014). Yet, many unknowns remain in our comprehension of ice-stream dynamics

25 (Tulaczyk et al., 2000; Robel et al., 2013), and the underlying processes governing ice flow are not sufficiently understood to successfully reproduce the NEGIS in sophisticated ice-sheet models (e.g. Mottram et al., 2019; Shepherd et al., 2020). The EastGRIP ice core sheds some light on the key processes, as it reveals unique information about ice dynamics, stress regimes, temperatures and basal properties, all of which are crucial components in ice-flow models.

Chemical and physical parameters measured in ice cores reflect the atmospheric conditions at the time and location of

30 deposition (e.g. Alley et al., 1993; Petit et al., 1999; Andersen et al., 2004; Marcott et al., 2014). Most of the deep drilling projects in Greenland and Antarctica are located in slow-moving areas at ice domes or near ice divides (e.g. GRIP (Dahl-Jensen et al., 1993), Dome Fuji (Ageta et al., 1998), Dome C (Parrenin et al., 2007)), where the ice core represents climate records from this fixed location. For ice cores drilled on the flank of an ice sheet (e.g. GISP2 (Meese et al., 1997), Vostok (Lorius et al., 1985; Petit et al., 1999)) or in areas with higher flow velocities (e.g. Camp Century (Dansgaard and Johnsen,

35 1969), Byrd (Gow et al., 1968), NorthGRIP (Andersen et al., 2004), EDML (Barbante et al., 2006), WAIS Divide (Fudge et al., 2013), NEEM (NEEM Community members et al., 2013)), the ice found at depth was originally deposited further upstream and advected with the lateral flow. The spatial variation in accumulation rate, surface temperature and atmospheric pressure in the upstream area can introduce non-climatic imprints in the ice core (e.g. Koutnik et al., 2016; Fudge et al., 2020). The magnitude of these upstream effects depends on the ice-flow velocity, spatially variable precipitation and the sensitivity to atmospheric

40 variations of the parameter under consideration. While well-mixed atmospheric gases, such as carbon dioxide or methane, and dry-deposited impurities are barely affected (Fudge et al., 2020), properties extracted from the ice phase can show significant bias which needs to be taken into account to ensure accurate data interpretation. Affected measurements include aerosols and cosmogenic isotopes, such as ^{10}Be (Yiou et al., 1997; Finkel and Nishiizumi, 1997; Raisbeck et al., 2007; Delaygue and Bard, 2011), the isotopic composition of water (Dansgaard, 1964; Jouzel et al., 1997; Aizen et al., 2006), the total air content

45 (Raynaud et al., 1997; Eicher et al., 2016) and ice temperatures (Salamatin et al., 1998). Processes such as vertical thinning of the ice column and firn densification are also influenced by upstream effects and have consequences on the annual layer thicknesses (Dahl-Jensen et al., 1993; Rasmussen et al., 2006; Svensson et al., 2008) and the age difference between ice and the enclosed air (Herron and Langway, 1980; Alley et al., 1982). Upstream effects in the EastGRIP ice core are expected to be particularly strong due to the fast ice flow in the upstream area (57 ma^{-1} at EastGRIP, Hvidberg et al., 2020), the strong

50 gradient in accumulation rate across Greenland's main ice ridge (Burgess et al., 2010) and the increasing elevation towards the central ice divide (Simonsen and Sørensen, 2017).

In this study, we use a two-dimensional Dansgaard–Johnsen model to simulate the ice flow along three approximated flow lines between the ice-sheet summit (GRIP) and EastGRIP. Model parameters are sampled during a Monte Carlo inversion by minimizing the misfit between modelled isochrones and isochrones observed in radio-echo-sounding (RES) images of known

55 depth and age. From the resulting flow model, we calculate particle trajectories backwards in time to determine the source area

of ice found in the EastGRIP ice core and estimate the accumulation rate at the time of deposition. The results presented here serve as a basis for corrections of upstream effects in various chemical and physical quantities. The inverted model parameters give insight into basal properties and ice-flow dynamics along the flow lines and can be used to constrain more sophisticated numerical models of the NEGIS.

2 Data and methods

2.1 EastGRIP flow lines

The upstream flow path of ice found in the EastGRIP ice core can be estimated from present-day surface velocities. Many high-resolution satellite-based velocity products are available. However, as a consequence of error propagation, minor uncertainties and bias in the data severely affect the tracking of flow lines along the velocity field (Hvidberg et al., 2020). We derived flow lines from different surface velocity products (e.g. Joughin et al., 2018; Gardner et al., 2020; Andersen et al., 2020, see Supplementary Material), and the diversity of these lines illustrates the uncertainties affecting along-flow tracking. The flow-line deviations between different products become considerably larger with increasing distance from EastGRIP as a result of error propagation and larger uncertainties attributed to slow-moving areas. Due to the small bias, we consider the DTU_SPACE (Andersen et al., 2020) line the most likely current flow line (Fig.1b). Yet, there is no evidence that the present-day velocity field was the same in the past. A slight shift in the NEGIS shear margins or the central ice divide, for instance, would have a large effect on the velocity field and, hence, the determination of the flow line through EastGRIP remains ambiguous.

The availability of RES data in the study area is limited, and unfortunately, the flight lines generally do not follow the surface velocity field. We have thus composed three approximated flow lines connecting the EastGRIP ($75.63°$ N, $35.99°$ W, 2720 m) and the GRIP ($72.58°$ N, $37.63°$ W, 3230 m) drill sites from the available RES data sets (Fig.1b). The downstream parts of profile A and B consist of the same flight line, which passes through the EastGRIP camp and crosses the southern shear margin around 82 km upstream of EastGRIP. Outside the NEGIS, the two lines split up and connect to two different RES profiles. Line B remains relatively close to the flow direction of the DTU_SPACE line but has a wide data gap in the centre of the profile. In line A, this problem is circumvented by using a radar profile connecting directly to GRIP, which has the consequence of a deviation from the observed surface flow field of more than 15 degrees in some parts. Profile C follows the NEGIS all the way to the central ice divide and connects to GRIP over the ice ridge without crossing the shear margin. To avoid uncertainties related to the proximity of the model boundaries, the flow lines were extended 50 km beyond EastGRIP and have a total length of 423 (line A), 422 (line B) and 480 km (line C).

The radar data used in this study (Table 1) were measured by the Alfred Wegener Institute (AWI, Jansen et al., 2020; Franke et al., in prep.) and the centre for Remote Sensing of Ice Sheets (CReSIS, 2020). The AWI data were recorded by an 8-antenna-element ultra-wideband radar system (MCoRDS5) mounted on the Polar 6 Basler BT-67 aircraft, operating at a frequency range of 180–210 MHz (Franke et al., 2020; Franke et al., in prep.). The CReSIS radar data were measured by a ICORDS 2 (1999) and MCoRDS 2 (2012) radar system, mounted on a P3 aeroplane, with a frequency range of 141.5–158.5 MHz and 180–210 MHz, respectively. Details of the three radar systems are provided in Table 2. To account for any differences in surface
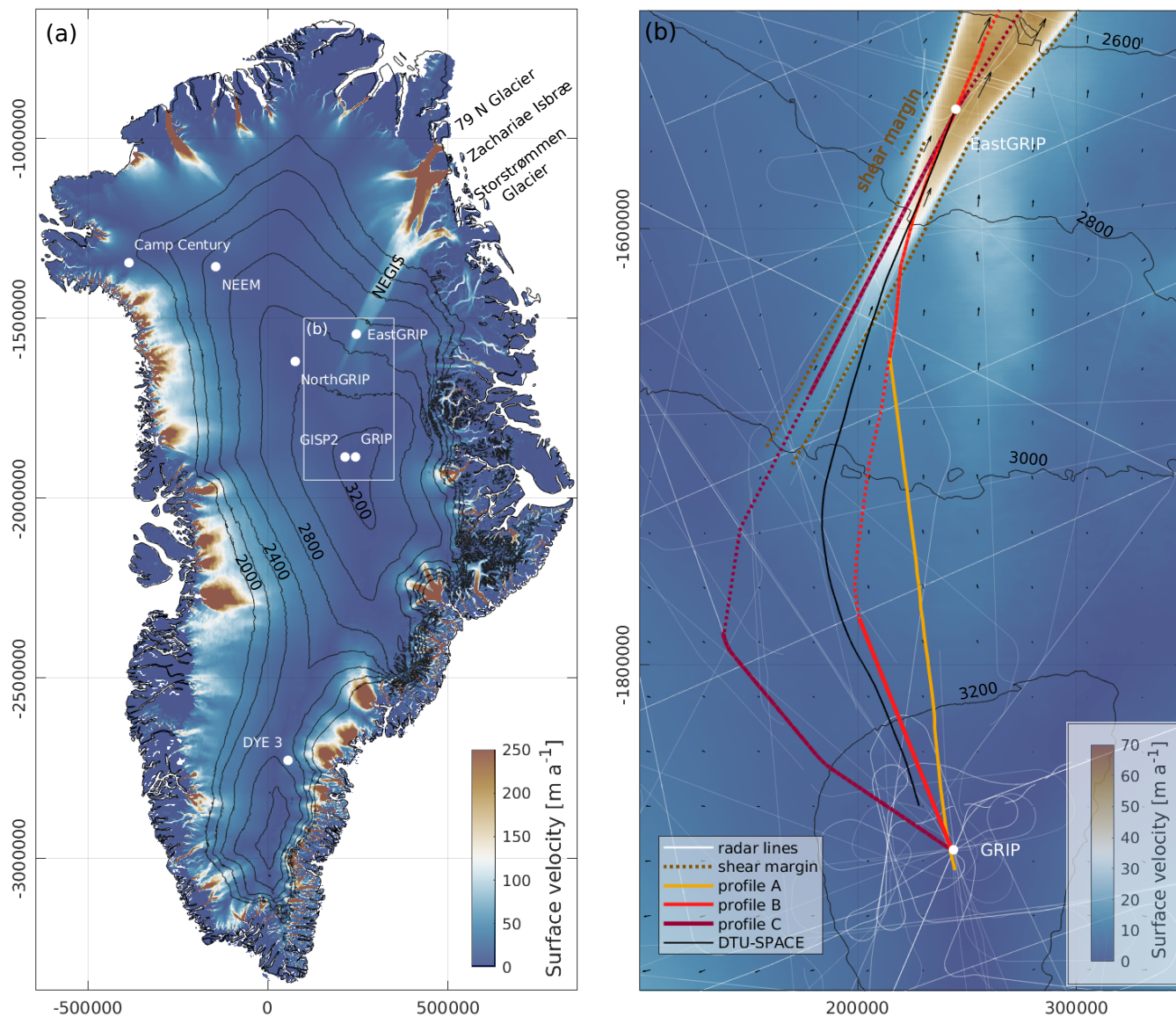
Figure 1. (a) Overview of past and ongoing deep ice-core drilling projects on the GrIS (surface elevation and Greenland contour lines by Simonsen and Sørensen, 2017; Greene et al., 2017) and the outline of the study area. The NEGIS appears as a distinct feature in the surface velocities (Joughin et al., 2018). It extends from the central ice divide to the northeastern coast, where it splits up into the three marine-terminating glaciers 79N Glacier, Zachariae Isbræ and Storstrømmen Glacier. **(b)** The present-day EastGRIP flow line is derived from the DTU_SPACE surface velocity product (Andersen et al., 2020). Due to the limited availability of radar data along the flow line, we construct three approximate flow lines through a combination of various radar products (profile A–C) between GRIP and EastGRIP. Flow line B and C lack data in the centre of the profiles, marked as a dashed line. The downstream parts of line A and B comprise the same radar profile, which crosses the southern shear margin 82 km upstream of EastGRIP.

elevation or topography between RES data from different years, the ice surface reflection of the radar profiles was aligned to
the surface elevation from the Arctic DEM (digital elevation model, Porter et al., 2018). The bed topography in the data gaps
of the profiles was derived from the BedMachine v3 data set (Morlighem et al., 2017).

Table 1. Radio-echo-sounding profiles used to approximate the EastGRIP flow lines A–C. The data sets were measured between 1999 and 2018 by the centre for Remote Sensing of Ice Sheets (CReSIS, University of Kansas, https://data.cresis.ku.edu/) and the Alfred Wegener Institute (AWI, Jansen et al., 2020; Franke et al., in prep.).

Flow line	Data files	Institution	Year	Radar system
A	Data_20180512_01_001 – 004	AWI	2018	MCoRDS 5
A	Data_19990512_01_009 – 010	CReSIS	1999	ICoRDS 2
B	Data_20180512_01_001 – 004	AWI	2018	MCoRDS 5
B	Data_19990523_01_016 – 017	CReSIS	1999	ICoRDS 2
C	Data_20180517_01_002 – 004	AWI	2018	MCoRDS 5
C	Data_20120330_03_008 – 011	CReSIS	2012	MCoRDS 2

Table 2. Operating parameters of the radar systems used for data acquisition. Further details can be found in Gogineni et al. (2001), Byers et al. (2012) and Franke et al., in prep..

Parameter	ICORDS 2	MCoRDS 2	MCoRDS 5
Bandwidth	141.5–158.5 MHz	180–210 MHz	180–210 MHz
Tx power	200 W	1050 W	6000 W
Waveform	Analogue chirp (SAW)	8 channel chirp (2–3 wave forms)	8 channel chirp (3 wave forms)
Sampling frequency	18.75 MHz	111 MHz	1600 MHz
Transmit channels	1	8	8
Receiving channels	1	15	8
Range resolution	7.6m	4.3m	4.3m

2.2 Stratigraphy

2.2.1 Extending the chronology of EastGRIP from GS-2 to GS-14

Mojtabavi et al. (2020) synchronized the EastGRIP and NorthGRIP ice cores for the last 15 kyr in order to apply the Greenland Ice Core Chronology 2005 (GICC05 Andersen et al., 2006) to EastGRIP. By 2019, the ice-core drilling progressed down to 2,122.45 m, allowing us to extend the time scale to 49.2 ka b2k (thousands of years before 2000 CE).

We identified common isochrones between EastGRIP, NorthGRIP and NEEM to transfer the GICC05 chronology to the EastGRIP record. This involved the same methods applied to NEEM by Rasmussen et al. (2013) and to the upper 1,383.84 m of EastGRIP by Mojtabavi et al. (2020). The isochrones chosen for synchronization purposes are mainly volcanic eruptions, which are registered as brief spikes in the electrical conductivity measurements (ECM, Hammer, 1980). The search of common ECM spikes was performed manually with a strong focus on finding patterns of similarly spaced eruptions rather than single and isolated events. The Matlab GUI 'Matchmaker' was used to visualize long data stretches and to evaluate the quality of the match (Rasmussen et al., 2013). An iterative multi-observer protocol was applied to reduce problems with confirmation bias and to ensure reproducibility of the match.

A total of 262 match points were identified between 1,383.84 m and 2,106.65 m, adding to the previously known 381 match points found above 1,383.84 m. The match points between EastGRIP and the other two cores are shown in Fig.2, representing all the volcanic tie points. The annual-layer-counted GICC05 chronology was transferred to EastGRIP by linear interpolation of depths between the match points. The age of the 1,383.84 m match point was already established to be 14,966 years b2k, which is near the termination of Greenland stadial GS-2, with a reported maximum counting error (MCE) of 196 years (Rasmussen et al., 2014). The age of the deepest match point was established to be 49,200 years b2k, just at the end of GS-14, with an MCE of 2,026 years.

As in earlier similar work (Rasmussen et al., 2013; Seierstad et al., 2014), very few match points were observed in the stadials, most clearly seen in Fig.2 in the long stadial stages of GS-2 and GS-3. Weakness of volcanic signals across stadial periods should not be attributed to a diminished global volcanic activity but rather to increased deposition of alkaline dust that neutralizes volcanic acid, caused by much colder and drier climatic conditions (Rasmussen et al., 2013). The largest distance between match points was observed across GS-2 and GS-3 and spans about 162 m of EastGRIP ice.

2.2.2 Isochrone tracing

Electromagnetic waves are sensitive to changes in dielectric permittivity and electrical conductivity. Contrasts in the dielectric properties of ice lead to so-called internal reflection horizons (IRH). In ice sheets, these contrasts typically can have three different origins: The permittivity varies with (1) density contrasts in the uppermost part of the ice column (Robin et al., 1969) or (2) changes in the crystal orientation fabric (Harrison, 1973), and the electrical conductivity of ice is altered by (3) impurity layers such as volcanic deposits (Paren and Robin, 1975). The latter is the most common reflector type below the firn (Millar, 1982; Eisen et al., 2006), and because it is related to layers deposited over a relatively short period, most internal reflections can be considered isochrones (Siegert, 1999; Hempel et al., 2000). Post-depositional deformation of isochrones provides information on ice-flow dynamics and can be used to reconstruct past and present flow characteristics.

We traced IRHs using a semi-automatic Matlab program. The algorithm is based on calculating the local slope in each pixel of the RES image by minimizing the variance along a local line segment. Layers are traced automatically between two user-defined points by following the steepest slope from both ends and subsequent weighting of the two lines by distance to the end points. The number of picks required for thorough tracing depends on the data quality and reflector strength. The total depth
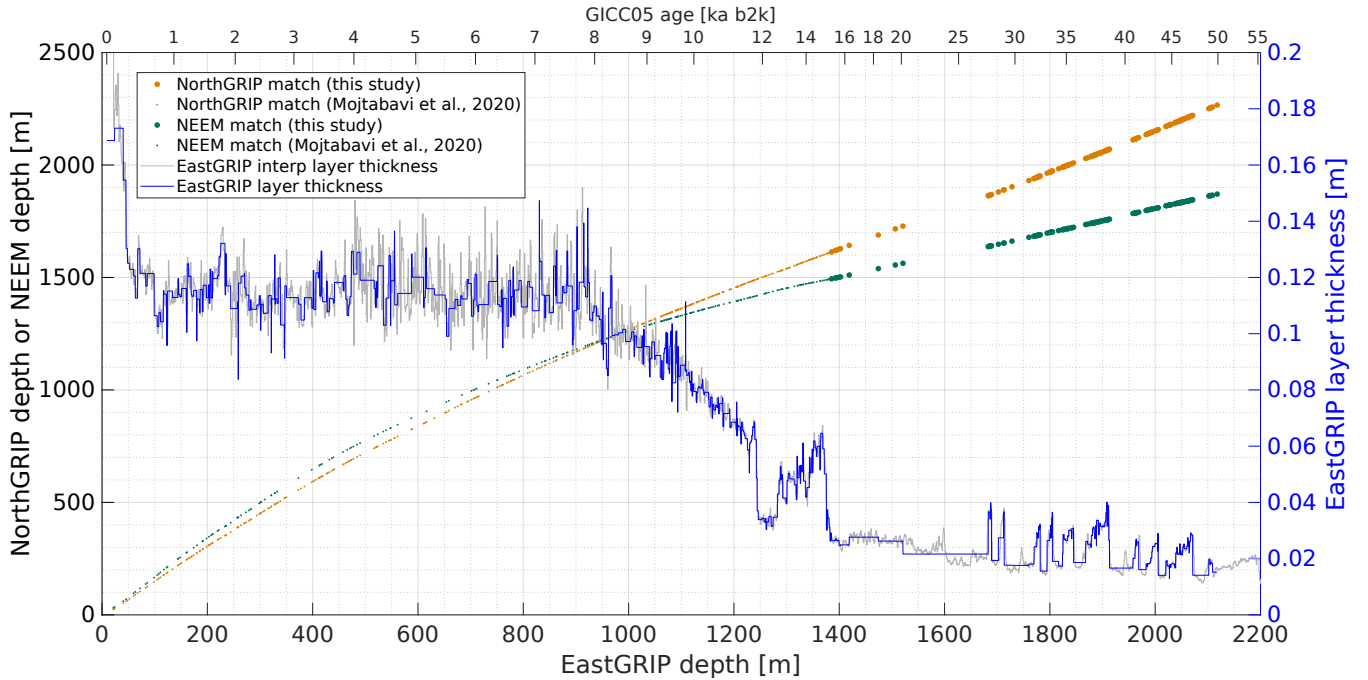
Figure 2. Synchronization between the EastGRIP, NorthGRIP and NEEM ice cores and comparison of match points obtained in this study with earlier results from Mojtabavi et al. (2020). The annual layer thickness of EastGRIP was computed after transferring GICC05 ages by linear interpolation to the EastGRIP ice core. The blue curve shows the annual layer thickness obtained by the match points only. The grey line indicates a high-resolution estimate of annual layer thicknesses at EastGRIP, obtained from the linear interpolation between the EastGRIP–NorthGRIP match points and assigning the interpolated EastGRIP depths to the NorthGRIP ages.

uncertainty was calculated as:

$$\tilde{z}_t = \sqrt{\tilde{z}_p^2 + \tilde{z}_{rr}^2}, \tag{1}$$

where the depth uncertainty introduced during the picking process, $\tilde{z}_p$, is estimated to be 10 m, and $\tilde{z}_{rr}$ is the radar range resolution of the corresponding RES image and defined as

$$\tilde{z}_{rr} = \frac{kc}{2B\sqrt{3.15}}, \tag{2}$$

135

where k is the window widening factor of 1.53, c is the speed of light, B is the radar bandwidth and 3.15 is the dielectric permittivity of ice.

The traced IRHs were dated by assigning the average reflector depth over ± 250 m around the trace closest to the GRIP and EastGRIP sites to the extended GICC05 time scale (Rasmussen et al., 2014; Seierstad et al., 2014; Mojtabavi et al., 2020). We

140 extrapolated this time scale at EastGRIP with 2 IRHs observed below the current bore-hole depth to obtain a tentative depth–age relationship between 2,106.65 m and the expected bed depth of 2,668.6 m. The total age uncertainty, $\tilde{a}_t$, was estimated by

following the approach described in MacGregor et al. (2015), where:

$$\tilde{a}_t = \sqrt{\tilde{a}_c^2 + \tilde{a}_{rr}^2 + \tilde{a}_p^2}, \tag{3}$$

takes into account the age uncertainties associated with the time scale ($\tilde{a}_c$, equivalent to 0.5 MCE), the radar range resolution

145   ($\tilde{a}_{rr}$), and the layer picking process ($\tilde{a}_p$). The uncertainties related to the range resolution are estimated with the following formula:

$$\tilde{a}_{rr} = \frac{1}{2} \sum |a_c(z \pm \tilde{z}_{rr}) - a_c(z)|, \tag{4}$$

where a_c is the ice-core age from the GICC05 time scale. Similar to Eq. (4), $\tilde{a}_p$ is estimated with

$$\tilde{a}_p = \frac{1}{2} \sum |a_c(z \pm \tilde{z}_p) - a_c(z)|. \tag{5}$$

150   ## 2.3   Ice flow model

A full simulation of ice flow in the catchment area of the NEGIS is a highly under-determined problem (Keisling et al., 2014), lacking geophysical, climatic and ice-core data, some of which will later become available. Simpler models do not solve the problem in detail and are thus computationally much cheaper. Limited but still useful information can be obtained from a simplified treatment of ice flow (e.g. Dansgaard and Johnsen, 1969; Dahl-Jensen et al., 2003; Waddington et al., 2007;

155   Christianson et al., 2013; Keisling et al., 2014). Here, we use a two-dimensional Dansgaard–Johnsen model (Dansgaard and Johnsen, 1969) to simulate the propagation of internal layers along approximated flow lines between the ice-sheet summit (GRIP) and EastGRIP. The simplicity of the model makes it well suited for the Monte Carlo method due to its few model parameters, the allowance for large time steps, and because it has an analytical solution (Grinsted and Dahl-Jensen, 2002). The model assumes ice incompressibility and a constant vertical strain rate down to the so-called kink height, h, below which the

160   strain rate decreases linearly. Basal sliding and melting are included in the model, and the ice-sheet thickness, H, is assumed to be constant in time. We consider a coordinate system where the x-axis points along the approximated flow line, the y-axis is horizontal and perpendicular to the flow line, and the z-axis indicates the height above the bed. The horizontal velocities parallel ($u_\parallel$) and perpendicular ($u_\perp$) to the profiles are described by Grinsted and Dahl-Jensen (2002) as:

$$u_\parallel(z) = \begin{cases} u_{\parallel,sur}(x,y)\left[(1-f_B)\frac{z}{h} + f_B\right], & z \in [0,h] \\ u_{\parallel,sur}(x,y), & z \in [h,H], \end{cases} \tag{6}$$

165

$$u_\perp(z) = \begin{cases} u_{\perp,sur}(x,y)\left[(1-f_B)\frac{z}{h} + f_B\right], & z \in [0,h] \\ u_{\perp,sur}(x,y), & z \in [h,H], \end{cases} \tag{7}$$

where $u_{\parallel,sur}$ and $u_{\perp,sur}$ are the surface velocities, and the basal sliding factor, f_B, is the ratio between the ice velocity at the bed and at the surface. Ice flow in the vicinity of an ice stream is affected by lateral compression and longitudinal extension, in

particular across the shear margins of the NEGIS.

170   We thus introduce $\alpha = \frac{\partial u_\parallel}{\partial x} + \frac{\partial u_\perp}{\partial y}$ as the sum of the horizontal strain rates, and due to ice incompressibility we can write $\alpha + \frac{\partial w}{\partial z} = 0$. The x and y dependency in Eq. (6 - 7) only relates to the surface velocity, such that α_{sur} represents the horizontal dependency in the equations. The vertical velocities (Dansgaard and Johnsen, 1969) are obtained through integration of the incompressibility relation $w(z) = -\int \alpha dz$:

$$\omega(z) = \begin{cases} \omega_{base} - \alpha_{sur}(f_B z + \frac{z^2}{2h}(1 - f_B)) & z \in [0, h] \\ \omega_{sur} + \alpha_{sur}(H - z) & z \in [h, H]. \end{cases} \tag{8}$$

175   The boundary conditions at the surface and bedrock are:

$$\omega_{base} = -\lambda_B + f_B u_{sur} \frac{\partial B}{\partial x} \tag{9}$$

$$\omega_{sur} = -\lambda_H + u_{sur} \frac{\partial S}{\partial x}, \tag{10}$$

where λ_B is the positive basal melt rate and λ_H is the positive accumulation rate. From Eq. (8) we derive the following expression for α_{sur}:

180    $$\alpha_{sur} = \frac{\omega_{base} - \omega_{sur}}{H - \frac{h}{2}(1 - f_B)}, \tag{11}$$

and the integration of Eq. (8) yields the isochrone depth–age relationship:

$$(H - z) = \frac{-\lambda_H}{\alpha_{sur}}(1 - e^{\alpha_{sur} t}), \tag{12}$$

where parameters z and t are the height and age of the isochrones. The unknowns λ_H and α_{sur} are obtained by a curve-fitting function, using at least 5 isochrones younger than 10 ka at each point along the flow line. The remaining initial flow parameters

185   are approximated as:

$$\lambda_{B,0} = e_1 \hat{\mathbf{u}}_{sur} \tag{13}$$

$$f_{B,0} = e_2 \hat{\mathbf{u}}_{sur} \tag{14}$$

$$h_0 = H \left(\frac{1}{2} - e_3 \hat{\mathbf{u}}_{sur} \right), \tag{15}$$

with the normalized surface velocities, $\hat{\mathbf{u}}_{sur}$, the ice thickness, H, and the estimated scaling factors $e_1 = 0.03$, $e_2 = 0.8$ and

190    $e_3 = 0.4$. To simulate the propagation of ice particles deposited at the surface of the GrIS, Eq. (6) and Eq. (8) are solved for the past 50 kyr at a time interval of 10 years.

2.4 Climate model

The accumulation rates and surface velocities are adjusted to the climate conditions of the corresponding time by a scaling factor $\xi(t)$ (Johnsen et al., 1995):

$$\xi(t) = e^{k_2(\delta^{18}O - \delta^{18}O_w) - \frac{1}{2}k_1(\delta^{18}O^2 - \delta^{18}O_w^2)},$$ (16)

with $\quad k_1 = \dfrac{c_w - c_c}{\delta^{18}O_w - \delta^{18}O_c}, \quad$ and $\quad k_2 = c_w - \delta^{18}O_w k_1.$

We use the water isotope $\delta^{18}O$ record from NorthGRIP (Andersen et al., 2004) due to its high temporal resolution, and $\delta^{18}O_w = -35.2\ ‰$ and $\delta^{18}O_c = -42\ ‰$ are typical isotope values for warm and cold periods. The unknown parameters c_w and c_c are defined as the relative slopes of the accumulation rates in warm (c_w) and cold (c_c) periods:

$$c_w = \frac{1}{\lambda_H} \frac{\partial \lambda_H}{\partial \delta^{18}O}\bigg|_{\delta^{18}O = \delta^{18}O_w}, \quad c_c = \frac{1}{\lambda_H} \frac{\partial \lambda_H}{\partial \delta^{18}O}\bigg|_{\delta^{18}O = \delta^{18}O_c},$$ (17)

which typically assume values between 0 and 2. Like Buchardt and Dahl-Jensen (2007), we find that $c_w = 0.15$ and $c_c = 0.10$ gives a good approximation of the past climate variations.

2.5 Monte Carlo sampling

The ice-flow parameters λ_H, λ_B, h and f_B form the multi-dimensional model space $\mathbf{m}$. The observed data, $\mathbf{d}_{obs}$, include the depth of eight selected isochrones of given age and α_{sur} determined from Eq. (12). The model and data space are related through a non-linear function $\mathbf{d} = g(\mathbf{m})$. The misfit between the observed and modelled data in iteration i is defined as:

$$S(\mathbf{m}) = \sum_i \frac{|\mathbf{d}_{obs}^i - \mathbf{d}_{model}^i|}{\sigma^i},$$ (18)

where σ describes the data uncertainty. The probability density in the model space typically shows a global maximum surrounded by a large number of local maxima representing other possible solutions (Mosegaard and Tarantola, 1995). The simplest approach to avoid being trapped in one of the local maxima is the global sampling of every point in the model space. However, the amount of model parameters and the non-linear nature of our problem makes this method computationally unfeasible. Monte Carlo methods allow sampling according to the posterior probability distribution in a more efficient way. In the inverse Monte Carlo strategy used here (Mosegaard and Tarantola, 1995), the current model, $\mathbf{m}_{curr}$, is perturbed by a random walk in the model space. The perturbation of the ice-flow parameters along the flow lines occurs at intervals of 10 km, which results in a total amount of 168 (flow line A and B) and 188 (flow line C) model parameters.

Using the Metropolis algorithm (Metropolis et al., 1953), the perturbed model is accepted with the probability

$$P_{accept} = \min\left(\frac{L(\mathbf{m}_{pert})}{L(\mathbf{m}_{curr})}, 1\right),$$ (19)

where the likelihood function is defined as $L(\mathbf{m}) = e^{-S(\mathbf{m})}$. Sampling starts after the burn-in phase, ensuring the statistical independence of model parameters. A threshold regularizes the maximum deviation from the initial model to avoid sampling outside a physically feasible range.

3 Results

3.1 Radar Stratigraphy

Table 3. Characteristics of the traced isochrones connecting the GRIP and EastGRIP ice-core sites. Displayed depths and ages are the average over the three flow lines. Depth uncertainties include the uncertainty related to the picking process and to the radar range resolution. Age uncertainties are related to the GICC05 time-scale uncertainties and isochrone depths. The bold layers and the EastGRIP ages were used for the Monte Carlo inversion.

Layer	GRIP depth [m]	EastGRIP depth [m]	GRIP age [yrs b2k]	EastGRIP age [yrs b2k]
1	733 ± 13	421 ± 11	3,618 ± 73	3,498 ± 94
2	**795 ± 13**	**471 ± 11**	**4,004 ± 74**	**3,945 ± 95**
3	925 ± 13	573 ± 11	4,885 ± 85	4,805 ± 93
4	**1,217 ± 13**	**838 ± 11**	**7,178 ± 106**	**7,139 ± 95**
5	1,262 ± 13	882 ± 11	7,575 ± 107	7,531 ± 95
6	**1,347 ± 13**	**968 ± 11**	**8,364 ± 122**	**8,321 ± 110**
7	1,374 ± 13	996 ± 11	8,637 ± 124	8,600 ± 113
8	1,533 ± 13	1,153 ± 11	10,407 ± 162	10,365 ± 149
9	**1,592 ± 13**	**1,208 ± 11**	**11,209 ± 181**	**11,140 ± 168**
10	1,663 ± 13	1,282 ± 11	12,891 ± 327	12,822 ± 290
11	**1,749 ± 13**	**1,355 ± 11**	**14,612 ± 281**	**14,350 ± 206**
12	**2,039 ± 13**	**1,704 ± 11**	**28,633 ± 840**	**28,522 ± 647**
13	**2,193 ± 13**	**1,903 ± 11**	**38,015 ± 994**	**37,914 ± 793**
14	**2,298 ± 13**	**2,035 ± 11**	**45,463 ± 1,189**	**45,174 ± 1,086**
15	2,395 ± 13	2,152 ± 11	52,602 ± 1,360	51,920 ± 1,240

We traced 15 IRHs connecting the EastGRIP and GRIP drill sites along three approximated flow lines. The chosen isochrones show distinct features which could be identified in all RES images and allowed us to trace isochrones across disruptions and
225 data gaps. Comparison of the isochrone depths at the ice-core locations obtained from different RES images permits to assess the quality of the tracing procedure. The high resolution of the radar images recorded in 2018 facilitates isochrone tracing, and the EastGRIP depths obtained from the two different AWI radar profiles agree within 1.5 m. At GRIP, the discrepancy between isochrone depths obtained from three different radar profiles can be up to 30 m, which is slightly above the combined depth uncertainty related to the picking process and the resolution of the RES images. Lower range resolution and signal-to-noise ratio
230 in older RES data introduce bias in isochrone identification, and although distinct isochrones were chosen, a miss-correlation between IRHs recorded by different radar systems can not be entirely excluded. Moreover, the CReSIS profiles do not precisely intersect at GRIP and deviate from each other. The radar traces closest to GRIP are thus found at slightly different locations

for the three RES images, which explains the higher discrepancy of radar layer depths.

The isochrone dating was conducted for each profile individually, and the obtained depths, ages and uncertainties were
235   averaged over the three lines. The deepest non-continuous layer which could be identified at EastGRIP is found at 2360 m
depth and is estimated to be 72,400 years old. The layer depth of the continuously traced IRHs ranges from 421 ± 11 to $2,152$
± 11 m at the EastGRIP location, corresponding to ages of $3,498 \pm 94$ to $51,920 \pm 1,240$ years b2k. Reflectors 1–9 were
deposited during the Holocene. The remaining reflectors are found in ice from the Last Glacial Period from which reflector 10
and 11 can be attributed to the onset of the Younger Dryas and the Bølling–Allerød. Due to computational reasons, we did not
240   use all 15 layers for the Monte Carlo inversion but picked eight isochrones with approximately equal vertical spacing (Table
3), and used the EastGRIP ages for our simulation of layer propagation. The relation between the GRIP and EastGRIP depths
of the traced IRHs fits well with the GICC05 time scale (Mojtabavi et al., 2020; Rasmussen et al., 2014), and the ages obtained
from the two drill sites agree within the uncertainties. We note that the layer dating at EastGRIP consistently leads to younger
ages than the dating at GRIP, which is a likely consequence of inaccuracies related to the transformation between ice-core and
245   radar depths.

3.2   Model parameters

Due to the highly under-determined nature of our inverse problem, a unique solution of model parameters does not exist. The
Monte Carlo sampling results in a number of possible models distributed according to the posterior probability. We present
the mean model parameters with the standard deviations and emphasize that the histograms of the posterior distributions are
250   important to understand the uncertainties of the parameter considered.

The flow-line characteristics and model parameters for each flow line are summarized in Fig.3. The radar profiles with
observed and modelled isochrones are displayed as a function of the distance from the EastGRIP borehole. Particle trajectories
were calculated from the simulated velocity field and indicate the source area of ice found at the modelled isochrone depth in
the EastGRIP ice core. The horizontal strain rates ($\dot{\varepsilon}_{xx}$, $\dot{\varepsilon}_{yy}$ and $\dot{\varepsilon}_{xy}$) were obtained from the MEaSUREs Multi-year v1 surface
255   velocity components (Joughin et al., 2018) parallel ($u_{\parallel}$) and perpendicular ($u_{\perp}$) to the approximated flow line. The strain rates
show mostly low, positive values along the flow lines with the exception of the shear-margin crossing in profile A and B, which
is characterized by longitudinal extension and lateral compression.

The central observed features are the following:

1.   The accumulation rate decreases with increasing distance from the central ice divide. In flow line A and B, we observe
260   a slight increase in the accumulation rate of ~ 4–5 % over the shear margin, followed by drop of ~ 25–30 % inside the
ice stream.

2.   The kink height fluctuates around the middle of the ice column in the vicinity of the ice divide and is drawn close to the
bed in the centre of the profiles, at $\sim$ -200 km. We observe a general increase in the kink height at $\sim$ -100 km and note
that it remains in the lower part of the ice column at EastGRIP.

10.5194/tc-2021-63
2021-02-23
Author(s) 2021. CC BY 4.0 License.
en
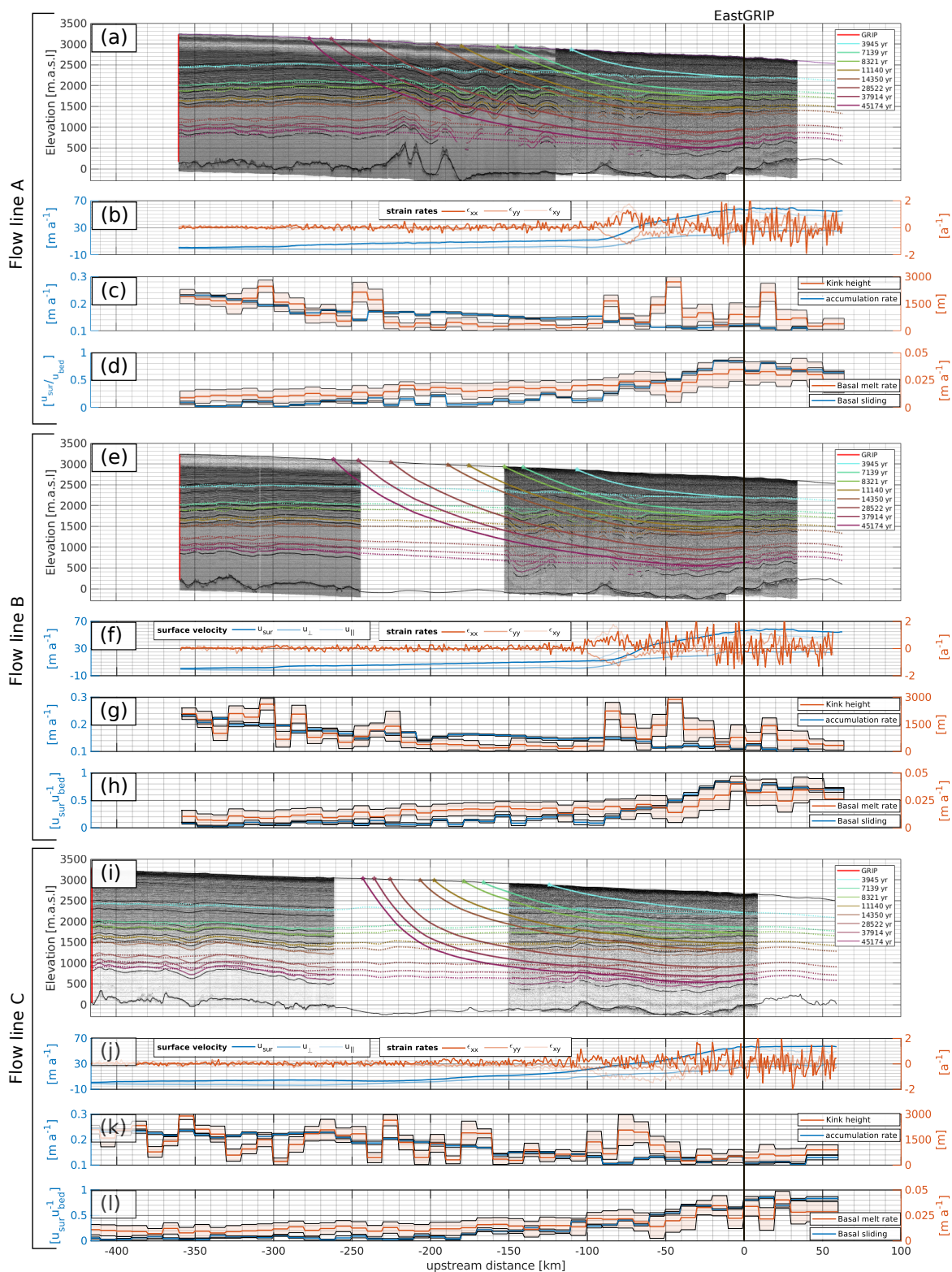
Figure 3. (Previous page.) Flow-line characteristics and model parameters for the approximated flow lines A **(a–d)**, B **(e–h)**, and C **(i–l)**. IRHs were traced in RES images and simulated with a two-dimensional Dansgaard–Johnsen model **(a, e, i)**. The horizontal strain rates at the surface were calculated from the MEaSUREs Multi-year v1 (Joughin et al., 2018) surface velocities **(b, f, j)**. The mean and standard deviations of the sampled model parameters accumulation rate, kink height, basal melt rate and basal sliding **(c, d, g, h, k, l)** were obtained from a Monte Carlo inversion by reducing the misfit between observed and simulated isochrones **(a, e, j)**. From the modelled velocity field we calculated particle trajectories backwards in time to obtain estimates of the source area location of snow deposition for specific depths in the EastGRIP ice core. All panels are aligned at EastGRIP and the x-axis indicates the distance from the borehole location.

265   3. The basal sliding velocity ranges between 0 and 30 % of the surface velocity outside the NEGIS and increases to 70–80 % at EastGRIP.

   4. The basal melt rates increase from 0–0.01 ma^{-1} at (GRIP) to 0.03–0.04 ma^{-1} at EastGRIP.

3.3   Monte Carlo Performance
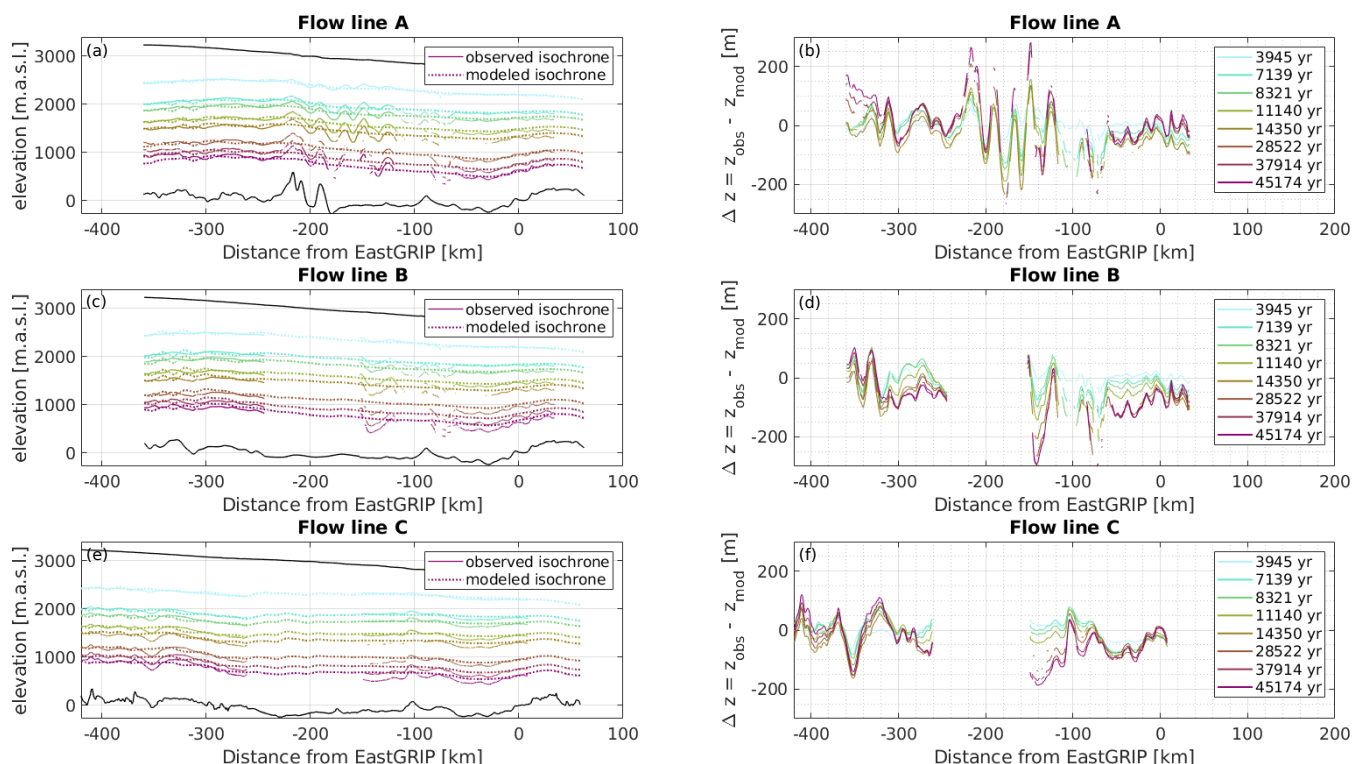
Figure 4. (a, c, e) Modelled and observed isochrones for profile A–C. The model fits the isochrones very well but fails to reproduce strong layer undulations over short distances. **(b, d, f)** Misfit between observed and modelled isochrone height: A positive misfit indicates that the modelled isochrone depth is overestimated.
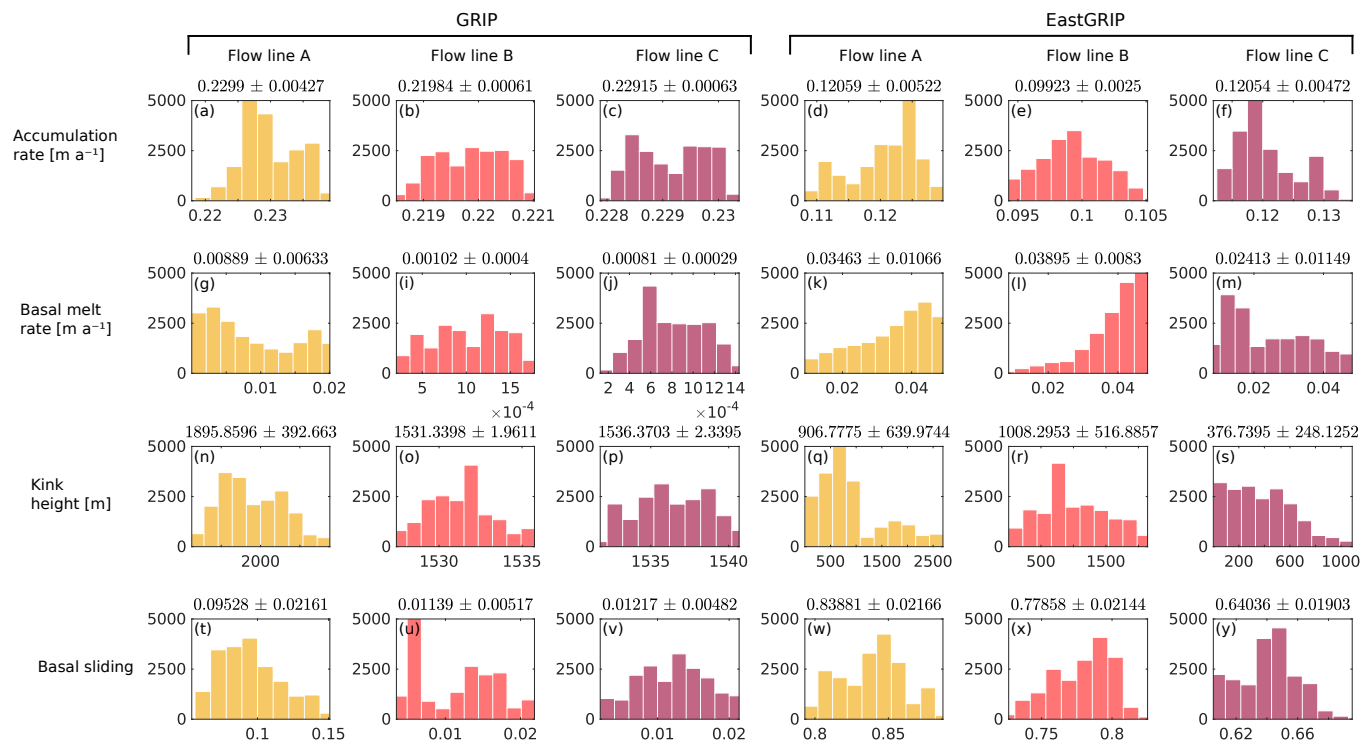
Figure 5. Histograms of model parameters accumulation rate, basal melt rate, kink height and basal sliding at GRIP and EastGRIP for each flow line. The corresponding means and standard deviations are displayed on top of the histograms.

The comparison of modelled and observed isochrones (Fig.4) shows a good fit in most parts of the flow lines. However, our model is not able to reproduce strong internal layer undulations which are not related to the bedrock topography or the surface conditions, resulting in a larger misfit where such undulations are present. The average misfit for flow line A, B and C is 4.56 %, 4.02 % and 3.16 % of the respective layer depth.

Histograms in Fig.5 show the sampled posterior probability distribution of model parameters at GRIP and EastGRIP with the corresponding mean and standard deviation displayed on top. Distributions with distinctive single peaks and low standard deviation point towards a good parameter resolution, while multiple maxima and high standard deviations indicate that several models are found to be equally likely. Exponential distributions imply that a parameter reaches regularization boundaries. These are most common in areas containing data gaps and strong isochrone undulations where regularization was necessary to constrain the parameters to a physically plausible range.

3.4 Ice origin and ice-flow history

From the modelled velocity field, we calculated particle trajectories backwards in time (Fig.3), which give insight into the source location and flow history of an ice particle found at a certain depth in the EastGRIP ice core, and allow us to determine

Table 4. Essential parameters for upstream corrections for selected depths of the EastGRIP ice core. The upstream distance, elevation and past accumulation rates, $\lambda_{H,past}$ describe the location of the source area and the conditions during ice deposition. $\lambda_{H,present}$ describes the present-day accumulation rates in the source area. All parameters are averages over the three flow lines.

Depth [m]	Age [yr b2k]	Upstream distance [km]	Elevation [m.a.s.l.]	Thinning function	$\lambda_{\mathbf{H,past}}$ [m a^{-1}]	$\lambda_{\mathbf{H,present}}$ [m a^{-1}]
100	665	52.0	2,759.2	0.12	0.128	0.121
200	1,553	78.7	2,799.2	0.21	0.143	0.139
300	2,418	96.2	2,838.1	0.26	0.148	0.143
400	3,322	108.3	2,858.8	0.22	0.143	0.150
600	5,037	129.7	2,894.4	0.28	0.160	0.150
800	6,805	150.8	2,927.9	0.38	0.159	0.154
1,000	8,640	169.5	2,949.3	0.42	0.157	0.165
1,200	11,015	187.0	2,968.6	0.32	0.102	0.171
1,400	15,571	204.0	2,997.2	0.52	0.053	0.161
1,600	23,382	220.9	3,032.9	0.60	0.062	0.172
1,800	33,524	237.2	3,058.1	0.67	0.093	0.179
2,000	43,107	254.8	3,083.2	0.77	0.112	0.173
2,200	54,487	271.5	3,108.0	0.77	0.051	0.197
2,400	73,563	286.0	3,125.7	0.78	0.042	0.186
2,600	95,808	297.4	3,142.4	0.94	0.161	0.199

the accumulation rate during its deposition (Fig 6). Due to the higher velocities in the ice stream, the source area of ice in the upper 1,600 m lies further upstream for flow line C compared to flow line A and B. For deeper ice, this trend is reversed, as the velocity along flow line C drops below the velocity of line A and B (Fig.6a). A similar effect manifests itself in the upstream

285 elevation, where higher velocities along flow line C result in higher elevations in the upper part of the ice column, which is compensated by a flatter topographic profile for ice deeper than 1,300 m (Fig.6b).

From the model-inferred in situ accumulation rates, $\lambda_{H,m}$, and annual layer thicknesses, λ_m, we calculate the ice-core thinning function γ:

$$\gamma = \frac{\lambda_{H,m} - \lambda_m}{\lambda_{H,m}}. \tag{20}$$

290 The thinning function increases almost linearly with depth but shows a considerable lower vertical thinning in the Younger Dryas and enhanced thinning in the Bølling–Allerød. The shift between the three lines results from the slightly different depth–age relationship and isochrone misfit obtained from the three profiles. We combine the thinning function with the annual
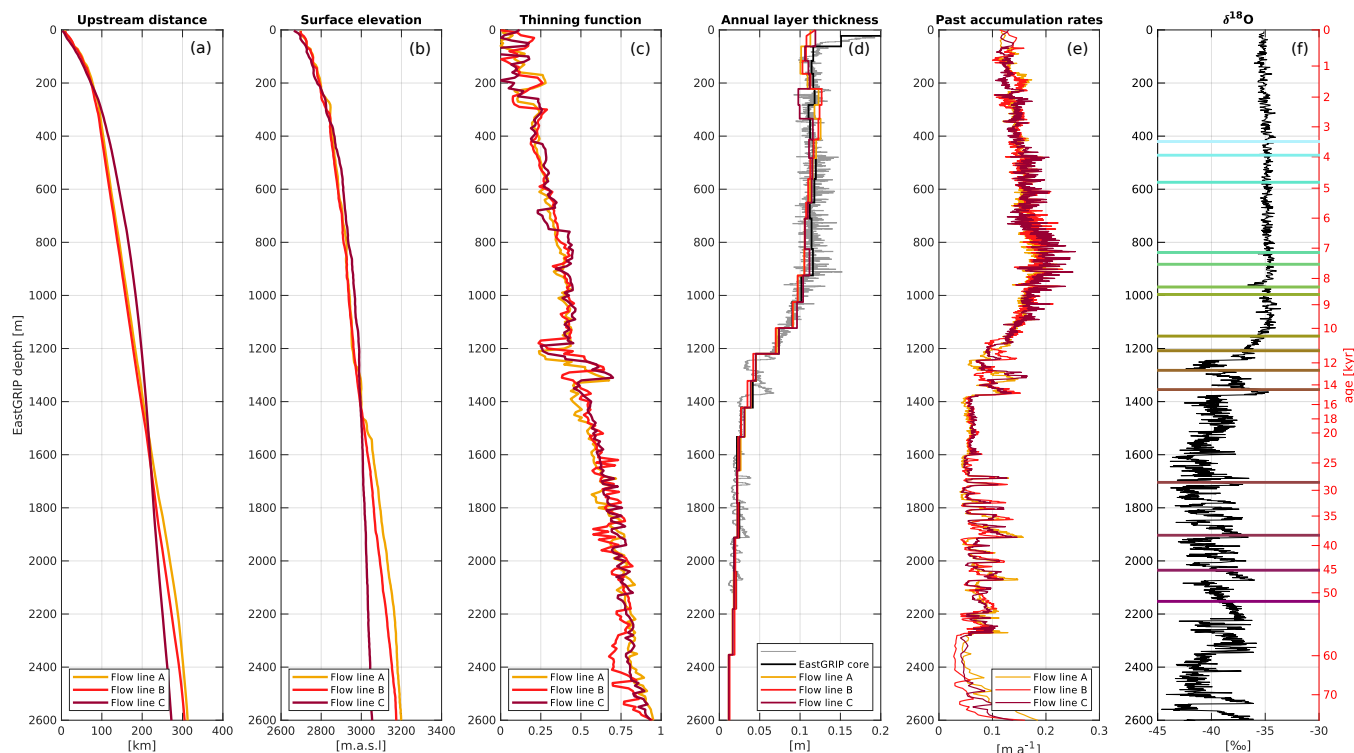
Figure 6. Modelled upstream distance (**a**) and surface elevation (**b**) of the source area for ice in the EastGRIP ice core. The thinning function (**c**) was calculated from the modelled accumulation rates and annual layer thicknesses (**d**) and was combined with the observed annual layer thicknesses (**d**) to calculate past accumulation rates in high resolution (**e**). The $\delta^{18}O$ curve from NorthGRIP (**f**) was scaled to the EastGRIP depths to put the results into a climatic context. Our model can reproduce the annual layer thicknesses observed in the EastGRIP ice core, indicating that our results are robust. The past accumulation rates at the deposition site increase with depth until 913 m, which compensates for the vertical thinning and produces the constant annual layer thicknesses observed during the past 8 kyr. Older ice was deposited under lower accumulation rates due to colder and dryer climatic conditions during the Last Glacial Period.

layer thicknesses observed in the EastGRIP ice core, λ_{obs}, to estimate past accumulation rates, $\lambda_{H,c}$:

$$\lambda_{H,c} = \frac{\lambda_{obs}}{1-\gamma}. \tag{21}$$

295 We find that the local accumulation rate at the deposition site increases from the present-day 0.12 ma^{-1} to a maximum of 0.242 ma^{-1} for ice at 913 m depth, which was deposited approximately 7,800 years ago. We note that the constant annual layer thicknesses observed in the upper 900 m of the EastGRIP ice core (Mojtabavi et al., 2020) coincides with the spatial pattern of increasing accumulation along the flow line in the upstream area. Ice between 900 m and 1,400 m is characterized by the transition from the Holocene into the Last Glacial Period with decreasing accumulation rates into the Younger Dryas

300 and a peak in the Bølling–Allerød. Older ice was, due to climatic reasons, deposited under lower accumulation rates between 0.05 ma^{-1} in the stadials and 0.14 ma^{-1} in the interstadials.

The accumulation-rate variations between the three flow lines are a combination of the varying along-flow accumulation pattern and upstream distance of the source area, and the model spread provides important uncertainty estimates. The average spread between the three accumulation rates is 5.2 % in the Holocene and 16.3 % in the Last Glacial Period. A maximum

305 deviation of 53 % is found at a depth of 2,541 m. We remark that, due to missing direct information on the annual layer thicknesses, accumulation rates below the current bore-hole depth of 2,122.45 m are based on tentative estimates and must be treated accordingly.

4 Discussion

4.1 Isochrone deformation and ice-flow parameters

310 Deformation of IRHs occurs as a consequence of bedrock topography (Robin and Millar, 1982; Jacobel et al., 1993), spatial variations in basal conditions (Weertman, 1976; Whillans, 1976; Whillans and Johnsen, 1983; Catania et al., 2010; Christianson et al., 2013; Leysinger Vieli et al., 2018; Wolovick et al., 2014), spatially varying accumulation rates and corresponding changes in ice-flow geometry (Dansgaard and Johnsen, 1969; Weertman, 1976; Whillans, 1976; Whillans and Johnsen, 1983), and as a consequence of convergent ice flow and ice-stream activity (Bons et al., 2016). Areas of enhanced basal melt rates

315 similarly drag down all the layers above, while variations in accumulation rate, kink height and basal sliding lead to depth-dependent deformation of the isochrones (Keisling et al., 2014).

The accumulation rates of $\sim$ 0.22–0.24 ma^{-1} at GRIP and $\sim$ 0.1–0.13 ma^{-1} at EastGRIP obtained in this study agree well with field observations (Dahl-Jensen et al., 1993; Vallelonga et al., 2014), and the low standard deviations point towards a robust solution. We find that the accumulation rates across the shear margins are 4–5% higher than outside the NEGIS and

320 25–30% higher than inside the ice stream (Fig.3c,g). Despite the low spatial resolution, our findings agree with Riverman et al. (2019), who found 20 % higher accumulation rates across the NEGIS shear margins compared to the surrounding. High stresses in the shear margins lead to a faster firn–ice transition and result in topographic depressions, which act as traps for additional drifting snow (Riverman et al., 2019).

The bed topography and bed lubrication have a considerable effect on ice-flow parameters. Flow over bed undulations af-

325 fect the elevation of internal layers due to variations in the longitudinal stresses within the ice (Hvidberg et al., 1997) and is often reflected in the surface topography (Cuffey and Paterson, 2010). If the bed is 'sticky', i.e. the basal sliding is small, the ice is compressed along the flow direction while vertically extended (Weertman, 1976), and IRHs are pushed upwards. At a slippery bed, the opposite is the case, resulting in along-flow extension of IRHs which leads to thinning and thus decreasing distance between the IRHs. Keisling et al. (2014) argued that major fold trains existing independently of bed undulations can

330 be explained by variations in the basal sliding conditions. This is, for instance, observed across shear margins, where local, steady state folds are formed as a response to the basal conditions (Keisling et al., 2014; Holschuh et al., 2014). In flow line A, we observe similar 'fold-trains' on a larger scale downstream of a substantial bed undulation (100–200 km upstream of EastGRIP). We argue that these strongly deformed isochrones are out-of-the-plane effects since they predominantly appear in parts of the flow lines which deviate from the observed surface velocity direction by more than 15 degrees. Accordingly, the

335 ice in the EastGRIP ice core is presumably not affected by them, and the fact that they are not reproduced by the model does not put any constraints on the usefulness of our results for upstream corrections.

The NEGIS differs from other ice streams in Greenland and Antarctica through the lack of clear lateral topographic constraints and high ice-flow velocities reaching exceptionally far inland. The positioning of the shear margins of the NEGIS are most likely strongly interconnected to the subglacial water system and the substrate and morphology of the bed (Christianson

340 et al., 2014; Franke et al., 2021). The vast amount of ice mass is added to the NEGIS by entering the ice stream through the shear margins (Franke et al., 2021). The distribution of available melt-water and a soft, deformable bed facilitate sliding and thus, ice flow acceleration at the NEGIS onset (Christianson et al., 2014). Evidence of a locally enhanced geothermal heat flux and basal ice at the melting point has been presented by e.g. Fahnestock et al. (2001) and MacGregor et al. (2016), and bed lubrication through melt-water production seems to be one of the driving mechanisms for rapid ice flow in the onset region of

345 the NEGIS (Smith-Johnsen et al., 2020). Our results support these previous findings in the following way: (1) Kink heights close to the bedrock imply that most shear deformation is happening in the lower part of the ice column or at the ice–bed interface.(2) Basal melt rates of 0.01 ma^{-1} or higher suggest that the basal ice temperatures along the flow lines are at the pressure melting point and enough energy is available to produce melt-water leading to substantial bed lubrication. (3) Basal sliding increases considerably along the flow lines and significantly contributes to the surface velocity at EastGRIP.

350 While it is commonly accepted that the NEGIS is initiated by a locally enhanced geothermal heat flux (e.g. Fahnestock et al., 2001; Alley et al., 2019), the magnitude thereof and the resulting hydrological conditions of the bed are still highly debated. Previous studies using simple strain-rate models in combination with radar stratigraphy indicate basal melt rates of 0.1 ma^{-1} or higher in the vicinity of EastGRIP (Fahnestock et al., 2001; Keisling et al., 2014; MacGregor et al., 2016). However, the accuracy of these findings is limited since the local layer approximation (Waddington et al., 2007) is not valid in the surrounding

355 of the NEGIS (Keisling et al., 2014; MacGregor et al., 2016). Remarkably high basal melt rates of 0.16–0.22 ma^{-1} are also suggested by a recent study (Zeising and Humbert, 2021) using an autonomous phase-sensitive radio-echo sounder (ApRES) at EastGRIP. Melt rates in these order of magnitudes would require an unusual high geothermal heat flux, immensely exceeding the continental background (Fahnestock et al., 2001; Bons et al., 2020).

Our results show that the average basal melt rate at EastGRIP over the past 50 kyr was around 0.033 ± 0.009 ma^{-1}, and

360 that consistently higher melt rates would cause too much basal mass loss to observe isochrones as old as 72,400 years in the RES images. Alley et al. (2019) discussed the interactions between the GrIS and the geothermal anomaly, presumably caused by the passage of Greenland over the Iceland hot spot (Lawver and Müller, 1994), and hypothesized that an exceptionally unsteady and inhomogeneous geothermal heat flux underneath northeast Greenland could arise through perturbations of the mantle stress regime caused by ice-sheet fluctuations. The geothermal heat flux in the onset region of the NEGIS might thus

365 have experienced substantial oscillations in the past, and basal melt rates today could differ from the temporal average over the past 50 kyr.

4.2 EastGRIP source area and upstream effects

The source region of ice in the EastGRIP ice core extends over $\sim$ 300 km upstream. Holocene ice characterizes the upper 1,244 m of the ice core and has been advected up to 189 km. The climatic conditions during the last 8 kyr remained nearly

370 constant with similar accumulation rates as today (Table 4). However, due to increasing precipitation towards the central ice divide, ice from the past 8 kyr was deposited under increasingly higher accumulation rates with increasing age. Our results indicate that this upstream effect happens to compensate for the vertical layer thinning and results in the constant annual layer thicknesses observed in the upper 900 m of the EastGRIP ice core (Mojtabavi et al., 2020). One possible conclusion of this peculiar observation is that snow depositions must have been advected from far enough upstream to allow the compensation of

375 vertical thinning by increased accumulation rates in the source area. This gives reason to the hypothesis that ice flow velocities in the past 8 ka must have been similarly fast as today, and that, therefore, the NEGIS has likely been active during this time. However, we believe that RES images and estimates of present-day accumulation rates along the EastGRIP flow line are necessary to evaluate this hypothesis further.

Between 8 ka b2k and the beginning of the Holocene, accumulation rates decreased at the deposition site due to increasingly

380 colder and dryer climatic conditions, as we go further back in time and transition into the GS-1. The most recent Glacial Period extends from 119,140 to 11,703 years b2k (Walker et al., 2009) and is characterized by Dansgaard–Oeschger events, abrupt transitions between cold stadial and relatively mild interstadial periods (Dansgaard et al., 1982; Johnsen et al., 1992) causing oscillations in the accumulation rates. Ice from the Last Glacial Period was deposited between 189 and 299 km upstream from EastGRIP under lower accumulation rates than today. The upstream effect of increasing precipitation towards the central ice

385 divide is varying less than in the Holocene, as the change in upstream location per kyr in the record is much smaller. The basal ice at EastGRIP could be more than 100 ka old and has been deposited within 60 km from the ice divide, under conditions which can be expected to be similar to those at NorthGRIP and GRIP.

Ice which is entering the NEGIS must somehow propagate through the shear margin, which is an important characteristic of ice flow in ice streams and might have left an imprint on the crystal fabric and texture of ice extracted at EastGRIP. Our

390 modelling results along flow line A and B indicate that ice below 231 m in the EastGRIP ice core has passed the shear margin 82 km from EastGRIP around 1,810 years ago. Slightly enhanced annual layer thicknesses observed at a depth of 230 m seem unrelated to short-term warmer and wetter climate and might thus be an effect of enhanced accumulation across the shear margin, supporting our results. However, flow lines derived from various surface velocity products show quite a large spread with shear-margin crossings between 97 and 152 km from EastGRIP, corresponding to depths between 324 and 826 m in the

395 ice core.

Our model shows surface elevations at the deposition site which are up to 459 m higher than EastGRIP at the corresponding time. Assuming a normal thermal and pressure gradient, this implies that ice was deposited under up to 2.9° C colder temperatures and up to 41 hPa lower pressure than conditions found at the bore-hole location at the time of deposition.

4.3 Limitations

The most important limitation of this study arises from lacking radar data parallel to the flow field in the upstream area of EastGRIP. The approximated flow lines deviate from the present-day surface flow field in some parts by more than 15 degrees, which introduces out-of-the-plane effects. Data gaps encumbered isochrone tracing and restricted the Monte Carlo method due to missing information in those areas.

405 By introducing the parameter α, our model accounts for lateral compression and extension on a first degree order, but does not capture the full complexity of the flow field across the shear margins. While these play an essential role in the ice-flow dynamics of the NEGIS (Holschuh et al., 2019) and are likely to have left an imprint on the ice found in the EastGRIP ice core, the full simulation of the flow field is not attempted for the purpose of upstream corrections.

The elevation of the source area was determined solely from the present-day ice-sheet surface elevation and did not take into 410 account past fluctuations in the ice-sheet thickness. In general, surface elevation changes are relatively minor in the interior areas of central Greenland (Marshall and Cuffey, 2000; Letréguilly et al., 1991). Yet, Vinther et al. (2009) found that the GRIP elevation might have been up to 200 m higher during the early Holocene than today. We did not take into account changes in the ice thickness due to the large uncertainties which would be introduced, particularly in the Last Glacial Period. Our estimates on the surface elevation of the source area must thus not be interpreted as absolute values but rather as relative changes with 415 respect to the surface elevation of EastGRIP at the corresponding time.

Lacking data and a general understanding of ice-sheet flow far back in time put up additional constraints, and due to the relatively recent discovery of the NEGIS (Fahnestock et al., 1993), little is known about its evolution in the past. Observations of surface elevation and ice-flow velocities imply that the downstream end of the NEGIS has entered a state of dynamic thinning after at least 25 years of stability (Khan et al., 2014). However, it is not clear for how long the NEGIS has been active and how 420 its catchment geometry changed over time. The assumption of a constant flow field throughout the past 50 kyr is thus the best currently available, but potentially inaccurate, estimate of the past flow regime.

Our results do not give clear evidence on which of the flow lines gives the best results for upstream corrections. Since the present-day EastGRIP flow line is likely located somewhere between flow line A and C, our results can be interpreted as the outer boundaries and we consider the average over the three flow lines the best estimate for the upstream flow characteristics 425 with the corresponding model spread as uncertainties.

5 Conclusions

We traced isochrones in RES images along three approximated EastGRIP flow lines connecting the EastGRIP and GRIP drill sites. A two-dimensional Dansgaard–Johnsen model was used to simulate the propagation of isochrones along these flow lines. The simplicity of our model allowed to invert for the ice-flow parameters accumulation rate, basal melt rate, kink height and 430 basal sliding fraction. The flow parameters obtained from the Monte Carlo inversion give helpful insight into basal properties and ice-flow dynamics and can be used to constrain large-scale ice-sheet models.

On the basis of our modelled two-dimensional velocity field, we calculated particle trajectories backwards in time to deter-

mine the deposition site of ice found in the EastGRIP ice core. We present estimates of the upstream distance, surface elevation and accumulation rate at the time and location of ice deposition. This is valuable and necessary information for interpreting

435 ice-core parameters, and to separate past climate variability from non-climatic bias introduced by upstream effects. Our studies show that spatially increasing accumulation rates along the flow line in the upstream area are mainly responsible for the constant annual layer thicknesses observed for the last 8 kyr in the EastGRIP ice core.

The lack of radar data along the EastGRIP flow line is the biggest limitation of this study. None of the three simulated flow lines accurately represents the present-day flow field but can be regarded as upper and lower limits framing the upstream

440 effects. The acquisition of further radar data along the NEGIS flow line in the future would provide more accurate and valuable insights into the flow history of the EastGRIP ice and the NEGIS.

Data availability. The CReSIS radio-echo-sounding images used for isochrone tracing are publicly available on https://data.cresis.ku.edu/. The RES data recorded by AWI will be available by Jansen et al. (2020) and described by (Franke et al., in prep.). The extended EastGRIP time scale, our derived and approximated flow lines and an extended version of Table 4 will be available on https://www.iceandclimate.nbi.

445 ku.dk/data/ and in the Supplementary Material.

Author contributions. DDJ and TAG designed and carried out the study. AG developed the code used for isochrone tracing. AG and CSH derived the EastGRIP flow lines. DJ was co-investigator for the AWI radar survey and acquired the data in the field. SF processed the radar data obtained during the EGRIP-NOR-2018 AWI flight campaign. SOR, GS and TAG synchronized the EastGRIP ice core with NorthGRIP and NEEM and extended the time scale to the current drill depth. TAG prepared the manuscript with the contribution of all co-authors.

450 *Competing interests.* The authors declare that they have no conflict of interest.

Acknowledgements. This work was supported by the Villum Investigator Project IceFlow (NR. 16572). EastGRIP is directed and organized by the Centre for Ice and Climate at the Niels Bohr Institute, University of Copenhagen. It is supported by funding agencies and institutions in Denmark (A. P. Møller Foundation, University of Copenhagen), USA (US National Science Foundation, Office of Polar Programs), Germany (Alfred Wegener Institute, Helmholtz Centre for Polar and Marine Research), Japan (National Institute of Polar Research and

455 Arctic Challenge for Sustainability), Norway (University of Bergen and Trond Mohn Foundation), Switzerland (Swiss National Science Foundation), France (French Polar Institute Paul-Emile Victor, Institute for Geosciences and Environmental research), Canada (University of Manitoba) and China (Chinese Academy of Sciences and Beijing Normal University). We acknowledge the use of data and data products from CReSIS generated with support from the University of Kansas, NASA Operation IceBridge grant NNX16AH54G, NSF grants ACI-1443054, OPP-1739003, and IIS-1838230, Lilly Endowment Incorporated, and Indiana METACyt Initiative. We also acknowledge the use of

460 the CReSIS toolbox from CReSIS generated with support from the University of Kansas, NASA Operation IceBridge grant NNX16AH54G, and NSF grants ACI-1443054, OPP-1739003, and IIS-1838230. We thank the crew of the research aircraft Polar 6 and system Engineer Lukas

Kandora for their work during the AWI flight campaign 2018 and express our gratitude to John Paden and Tobias Binder, who helped with the data acquisition during the AWI survey. Sune Olander Rasmussen and Giulia Sinnl gratefully acknowledge the Carlsberg Foundation for supporting the project ChronoClimate. This research was enabled in part by computing facilities and support provided by WestGrid (www.westgrid.ca) and Compute Canada Calcul Canada (www.computecanada.ca). The scientific colour maps 'hawaii' and 'vik' (Crameri, 2020) are used in this study to prevent visual distortion of the data and exclusion of readers with colourvision deficiencies (Crameri et al., 2020).

References

Ageta, Y., Azuma, N., Fujii, Y., Fujino, K., Fujita, S., Furukawa, T., Hondoh, T., Kameda, T., Kamiyama, K., Katagiri, K., Kawada, K.,
470   Kawamura, T., Kobayashi, S., Mae, S., Maeno, H., Miyahara, T., Motoyama, H., Nakayama, Y., Naruse, R., Nishio, F., Saitoh, K.,
Saitoh, T., Shimbori, K., Shiraiwa, T., Shoji, H., Takahashi, A., Takahashi, S., Tanaka, Y., Yokoyama, K., and Watanabe, O.: Deep
ice-core drilling at Dome Fuji and glaciological studies in east Dronning Maud Land, Antarctica, Annals of Glaciology, 27, 333–337,
https://doi.org/10.3189/1998aog27-1-333-337, 1998.

Aizen, V. B., Aizen, E. M., Joswiak, D. R., Fujita, K., Takeuchi, N., and Nikitin, S. A.: Climatic and atmospheric circulation
475   pattern variability from ice-core isotope/geochemistry records (Altai, Tien Shan and Tibet), Annals of Glaciology, 43, 49–60,
https://doi.org/10.3189/172756406781812078, 2006.

Alley, R. B., Bolzan, J. F., and Whillans, I. M.: Polar firn densification and grain growth, Annals of Glaciology, 3, 7–11,
https://doi.org/doi:10.3189/S0260305500002433, 1982.

Alley, R. B., Meese, D. A., Shuman, C. A., Gow, A. J., Taylor, K. C., Grootes, P. M., White, J. W., Ram, M., Waddington, E. D., Mayewski,
480   P. A., and Zielinski, G. A.: Abrupt increase in Greenland snow accumulation at the end of the Younger Dryas event, Nature, 362, 527–529,
https://doi.org/10.1038/362527a0, 1993.

Alley, R. B., Pollard, D., Parizek, B. R., Anandakrishnan, S., Pourpoint, M., Stevens, N. T., MacGregor, J. A., Christianson, K., Muto, A.,
and Holschuh, N.: Possible Role for Tectonics in the Evolving Stability of the Greenland Ice Sheet, Journal of Geophysical Research:
Earth Surface, 124, 97–115, https://doi.org/10.1029/2018JF004714, 2019.

485   Andersen, J. K., Kusk, A., Boncori, J. P. M., Hvidberg, C. S., and Grinsted, A.: Improved ice velocity measurements with Sentinel-1 TOPS
interferometry, Remote Sensing, 12, 1–22, https://doi.org/10.3390/rs12122014, 2020.

Andersen, K. K., Azuma, N., Barnola, J. M., Bigler, M., Biscaye, P., Caillon, N., Chappellaz, J., Clausen, H. B., Dahl-Jensen, D., Fischer, H.,
Flückiger, J., Fritzsche, D., Fujii, Y., Goto-Azuma, K., Grønvold, K., Gundestrup, N. S., Hansson, M., Huber, C., Hvidberg, C. S., Johnsen,
S. J., Jonsell, U., Jouzel, J., Kipfstuhl, S., Landais, A., Leuenberger, M., Lorrain, R., Masson-Delmotte, V., Miller, H., Motoyama, H.,
490   Narita, H., Popp, T., Rasmussen, S. O., Raynaud, D., Rothlisberger, R., Ruth, U., Samyn, D., Schwander, J., Shoji, H., Siggard-Andersen,
M. L., Steffensen, J. P., Stocker, T., Sveinbjörnsdóttir, A. E., Svensson, A., Takata, M., Tison, J. L., Thorsteinsson, T., Watanabe, O.,
Wilhelms, F., and White, J. W.: High-resolution record of Northern Hemisphere climate extending into the last interglacial period, Nature,
431, 147–151, https://doi.org/10.1038/nature02805, 2004.

Andersen, K. K., Svensson, A., Johnsen, S. J., Rasmussen, S. O., Bigler, M., Röthlisberger, R., Ruth, U., Siggaard-Andersen, M. L., Peder
495   Steffensen, J., Dahl-Jensen, D., Vinther, B. M., and Clausen, H. B.: The Greenland Ice Core Chronology 2005, 15-42 ka. Part 1: construct-
ing the time scale, Quaternary Science Reviews, 25, 3246–3257, https://doi.org/10.1016/j.quascirev.2006.08.002, 2006.

Barbante, C., Barnola, J. M., Becagli, S., Beer, J., Bigler, M., Boutron, C., Blunier, T., Castellano, E., Cattani, O., Chappellaz, J., Dahl-Jensen,
D., Debret, M., Delmonte, B., Dick, D., Falourd, S., Faria, S., Federer, U., Fischer, H., Freitag, J., Frenzel, A., Fritzsche, D., Fundel, F.,
Gabrielli, P., Gaspari, V., Gersonde, R., Graf, W., Grigoriev, D., Hamann, I., Hansson, M., Hoffmann, G., Hutterli, M. A., Huybrechts,
500   P., Isaksson, E., Johnsen, S., Jouzel, J., Kaczmarska, M., Karlin, T., Kaufmann, P., Kipfstuhl, S., Kohno, M., Lambert, F., Lambrecht, A.,
Lambrecht, A., Landais, A., Lawer, G., Leuenberger, M., Littot, G., Loulergue, L., Lüthi, D., Maggi, V., Marino, F., Masson-Delmotte,
V., Meyer, H., Miller, H., Mulvaney, R., Narcisi, B., Oerlemans, J., Oerter, H., Parrenin, F., Petit, J. R., Raisbeck, G., Raynaud, D.,
Röthlisberger, R., Ruth, U., Rybak, O., Severi, M., Schmitt, J., Schwander, J., Siegenthaler, U., Siggaard-Andersen, M. L., Spahni, R.,
Steffensen, J. P., Stenni, B., Stocker, T. F., Tison, J. L., Traversi, R., Udisti, R., Valero-Delgado, F., Van Den Broeke, M. R., Van De

505   Wal, R. S., Wagenbach, D., Wegner, A., Weiler, K., Wilhelms, F., Winther, J. G., and Wolff, E.: One-to-one coupling of glacial climate variability in Greenland and Antarctica, Nature, 444, 195–198, https://doi.org/10.1038/nature05301, 2006.

Bons, P. D., Jansen, D., Mundel, F., Bauer, C. C., Binder, T., Eisen, O., Jessell, M. W., Llorens, M. G., Steinbach, F., Steinhage, D., and Weikusat, I.: Converging flow and anisotropy cause large-scale folding in Greenland's ice sheet, Nature Communications, 7, 1–6, https://doi.org/10.1038/ncomms11427, 2016.

510   Bons, P. D., de Riese, T., Franke, S., Llorens, M.-G., Sachau, T., Stoll, N., Weikusat, I., and Zhang, Y.: Comment on "Exceptionally high heat flux needed to sustain the Northeast Greenland Ice Stream" by S. Smith-Johnson et al., The Cryosphere, 14, 841–854, 2020, The Cryosphere Discussions, 2020, 1–5, https://doi.org/10.5194/tc-2020-339, 2020.

Buchardt, S. L. and Dahl-Jensen, D.: Estimating the basal melt rate at NorthGRIP using a Monte Carlo technique, Annals of Glaciology, 45, 137–142, https://doi.org/10.3189/172756407782282435, 2007.

515   Burgess, E. W., Forster, R. R., Box, J. E., Mosley-Thompson, E., Bromwich, D. H., Bales, R. C., and Smith, L. C.: A spatially calibrated model of annual accumulation rate on the Greenland Ice Sheet (1958-2007), Journal of Geophysical Research: Earth Surface, 115, 1–14, https://doi.org/10.1029/2009JF001293, 2010.

Byers, K. J., Harish, A. R., Seguin, S. A., Leuschen, C. J., Rodriguez-Morales, F., Paden, J., Arnold, E. J., and Hale, R. D.: A modified wideband dipole antenna for an airborne VHF ice-penetrating radar, IEEE Transactions on Instrumentation and Measurement, 61, 1435–
520   1444, https://doi.org/10.1109/TIM.2011.2181780, 2012.

Catania, G., Hulbe, C., and Conway, H.: Grounding-line basal melt rates determined using radar-derived internal stratigraphy, Journal of Glaciology, 56, 545–554, https://doi.org/10.3189/002214310792447842, 2010.

Christianson, K., Parizek, B. R., Alley, R. B., Horgan, H. J., Jacobel, R. W., Anandakrishnan, S., Keisling, B. A., Craig, B. D., and Muto, A.: Ice sheet grounding zone stabilization due to till compaction, Geophysical Research Letters, 40, 5406–5411,
525   https://doi.org/10.1002/2013GL057447, 2013.

Christianson, K., Peters, L. E., Alley, R. B., Anandakrishnan, S., Jacobel, R. W., Riverman, K. L., Muto, A., and Keisling, B. A.: Dilatant till facilitates ice-stream flow in northeast Greenland, Earth and Planetary Science Letters, 401, 57–69, https://doi.org/10.1016/j.epsl.2014.05.060, 2014.

Crameri, F.: Scientific colour maps, https://doi.org/10.5281/zenodo.4153113, 2020.

530   Crameri, F., Shephard, G. E., and Heron, P. J.: The misuse of colour in science communication, Nature Communications, 11, 1–10, https://doi.org/10.1038/s41467-020-19160-7, 2020.

CReSIS: Radar Depth Sounder Data Products, Lawrence, Kansas, USA, http://data.cresis.ku.edu/, 2020.

Cuffey, K. M. and Paterson, W. S. B.: The physics of glaciers, Butterworth-Heinemann/Elsevier, Amsterdam, 4. ed. edn., 2010.

Dahl-Jensen, D., Johnsen, S. J., Hammer, C. U., Clausen, H. B., and Jouzel, J.: Past Accumulation rates derived from observed annual
535   layers in the GRIP ice core from Summit, Central Greenland, Ice in the Climate System, 112, 517–532, https://doi.org/10.1007/978-3-642-85016-5_29, 1993.

Dahl-Jensen, D., Gundestrup, N., Gogineni, S. P., and Miller, H.: Basal melt at NorthGRIP modeled from borehole, ice-core and radio-echo sounder observations, Annals of Glaciology, 37, 207–212, https://doi.org/10.3189/172756403781815492, 2003.

Dansgaard, W.: Stable isotopes in precipitation, Tellus, 16, 436–468, https://doi.org/10.3402/tellusa.v16i4.8993, 1964.

540   Dansgaard, W. and Johnsen, S. J.: A Flow Model and a Time Scale for the Ice Core from Camp Century, Greenland, Journal of Glaciology, 8, 215–223, https://doi.org/10.3189/s0022143000031208, 1969.

Dansgaard, W., Clausen, H. B., Gundestrup, N., Hammer, C. U., Johnsen, S. F., Kristinsdottir, P. M., and Reeh, N.: A new Greenland deep ice core, Science, 218, 1273–1277, https://doi.org/10.1126/science.218.4579.1273, 1982.

Delaygue, G. and Bard, E.: An Antarctic view of Beryllium-10 and solar activity for the past millennium, Climate Dynamics, 36, 2201–2218,
545   https://doi.org/10.1007/s00382-010-0795-1, 2011.

Eicher, O., Baumgartner, M., Schilt, A., Schmitt, J., Schwander, J., Stocker, T. F., and Fischer, H.: Climatic and insolation control on the high-resolution total air content in the NGRIP ice core, Climate of the Past, 12, 1979–1993, https://doi.org/10.5194/cp-12-1979-2016, 2016.

Eisen, O., Wilhelms, F., Steinhage, D., and Schwander, J.: Improved method to determine radio-echo sounding reflector depths from ice-core
550   profiles of permittivity and conductivity, Journal of Glaciology, 52, 299–310, https://doi.org/10.3189/172756506781828674, 2006.

Fahnestock, M., Bindschadler, R., Kwok, R., and Jezek, K.: Greenland Ice Sheet surface properties and ice dynamics from ERS-1 SAR imagery, https://doi.org/10.1126/science.262.5139.1530, 1993.

Fahnestock, M., Abdalati, W., Joughin, I., Brozena, J., and Gogineni, P.: High geothermal heat flow, basal melt, and the origin of rapid ice flow in central Greenland, Science, 294, 2338–2342, https://doi.org/10.1126/science.1065370, 2001.

555   Finkel, R. C. and Nishiizumi, K.: Beryllium 10 concentrations in the Greenland Ice Sheet Project 2 ice core from 3-40 ka, Journal of Geophysical Research: Oceans, 102, 26 699–26 706, https://doi.org/10.1029/97JC01282, 1997.

Franke, S., Binder, T., Jansen, D., Paden, J. D., Dörr, N., Gerber, T. A., Miller, H., Helm, V., Steinhage, D., and Eisen, O.: Earth System Science Data, in preparation.

Franke, S., Jansen, D., Binder, T., Dörr, N., Helm, V., Paden, J., Steinhage, D., and Eisen, O.: Bed topography and subglacial landforms in
560   the onset region of the Northeast Greenland Ice Stream, Annals of Glaciology, 61, 143–153, https://doi.org/10.1017/aog.2020.12, 2020.

Franke, S., Jansen, D., Beyer, S., Neckel, N., Binder, T., Paden, J., and Eisen, O.: Complex basal conditions and their influence on ice flow at the onset of the Northeast Greenland Ice Stream, Journal of Geophysical Research: Earth Surface, 126, https://doi.org/10.1029/2020jf005689, 2021.

Fudge, T. J., Steig, E. J., Markle, B. R., Schoenemann, S. W., Ding, Q., Taylor, K. C., McConnell, J. R., Brook, E. J., Sowers, T., White,
565   J. W., Alley, R. B., Cheng, H., Clow, G. D., Cole-Dai, J., Conway, H., Cuffey, K. M., Edwards, J. S., Lawrence Edwards, R., Edwards, R., Fegyveresi, J. M., Ferris, D., Fitzpatrick, J. J., Johnson, J., Hargreaves, G., Lee, J. E., Maselli, O. J., Mason, W., McGwire, K. C., Mitchell, L. E., Mortensen, N., Neff, P., Orsi, A. J., Popp, T. J., Schauer, A. J., Severinghaus, J. P., Sigl, M., Spencer, M. K., Vaughn, B. H., Voigt, D. E., Waddington, E. D., Wang, X., and Wong, G. J.: Onset of deglacial warming in West Antarctica driven by local orbital forcing, Nature, 500, 440–444, https://doi.org/10.1038/nature12376, 2013.

570   Fudge, T. J., Lilien, D. A., Koutnik, M., Conway, H., Stevens, C. M., Waddington, E. D., Steig, E. J., Schauer, A. J., and Holschuh, N.: Advection and non-climate impacts on the South Pole Ice Core, Climate of the Past, 16, 819–832, https://doi.org/10.5194/cp-16-819-2020, 2020.

Gardner, A. S., Fahnestock, M. A., and Scambos, T. A.: ITS_LIVE Regional Glacier and Ice Sheet Surface Velocities, https://doi.org/10.5067/6II6VW8LLWJ7, 2020.

575   Gogineni, S., Tammana, D., Braaten, D., Leuschen, C., Akins, T., Legarsky, J., Kanagaratnam, P., Stiles, J., Allen, C., and Jezek, K.: Coherent radar ice thickness measurements over the Greenland ice sheet, Journal of Geophysical Research Atmospheres, 106, 33 761–33 772, https://doi.org/10.1029/2001JD900183, 2001.

Gow, A. J., Ueda, H. T., and Garfield, D. E.: Antarctic ice sheet: Preliminary results of first core hole to bedrock, Science, 161, 1011–1013, https://doi.org/10.1126/science.161.3845.1011, 1968.

580   Greene, C. A., Gwyther, D. E., and Blankenship, D. D.: Antarctic Mapping Tools for Matlab, Computers & Geosciences, 104, 151–157, https://doi.org/10.1016/j.cageo.2016.08.003, https://doi.org/10.1016%2Fj.cageo.2016.08.003, 2017.

Grinsted, A. and Dahl-Jensen, D.: A Monte Carlo-tuned model of the flow in the NorthGRIP area, Annals of Glaciology, 35, 527–530, https://doi.org/10.3189/172756402781817130, 2002.

Hammer, C. U.: Acidity of Polar Ice Cores in Relation to Absolute Dating, Past Volcanism, and Radio–Echoes, Journal of Glaciology, 25,
585   359–372, https://doi.org/10.3189/s0022143000015227, 1980.

Harrison, C. H.: Radio Echo Sounding of Horizontal Layers in Ice, Journal of Glaciology, 12, 383–397, https://doi.org/10.3189/s0022143000031804, 1973.

Hempel, L., Thyssen, F., Gundestrup, N., Clausen, H. B., and Miller, H.: A comparison of radio-echo sounding data and electrical conductivity of the GRIP ice core, Journal of Glaciology, 46, 369–374, https://doi.org/10.3189/172756500781833070, 2000.

590   Herron, M. M. and Langway, C. C.: Firn densification: an empirical model., Journal of Glaciology, 25, 373–385, https://doi.org/10.1017/S0022143000015239, 1980.

Holschuh, N., Christianson, K., and Anandakrishnan, S.: Power loss in dipping internal reflectors, imaged using ice-penetrating radar, Annals of Glaciology, 55, 49–56, https://doi.org/10.3189/2014AoG67A005, 2014.

Holschuh, N., Lilien, D. A., and Christianson, K.: Thermal Weakening, Convergent Flow, and Vertical Heat Transport in the Northeast
595   Greenland Ice Stream Shear Margins, Geophysical Research Letters, 46, 8184–8193, https://doi.org/10.1029/2019GL083436, 2019.

Hvidberg, C., Grinsted, A., Dahl-Jensen, D., Khan, S. A., Kusk, A., Andersen, J. K., Neckel, N., Solgaard, A., Karlsson, N., Kjær, H. A., and Vallelonga, P.: Surface velocity of the Northeast Greenland Ice Stream (NEGIS): Assessment of interior velocities derived from satellite data by GPS, The Cryosphere Discussions, pp. 1–27, https://doi.org/10.5194/tc-2020-103, 2020.

Hvidberg, C. S., Keller, K., Gundestrup, N. S., Tscherning, C. C., and Forsberg, R.: Mass balance and surface movement of the Greenland
600   ice sheet at summit, Central Greenland, Geophysical Research Letters, 24, 2307–2310, https://doi.org/10.1029/97GL02280, 1997.

Jacobel, R. W., Gades, A. M., Gottschling, D. L., Hodge, S. M., and Wright, D. L.: Interpretation of radar-detected internal layer folding in West Antarctic ice streams, Journal of Glaciology, 39, 528–537, https://doi.org/10.1017/s0022143000016427, 1993.

Jansen, D., Franke, S., Binder, T., Paden, J. D., Steinhage, D., Helm, V., and Eisen, O.: AWI UWB radar data along ice flow upstream of the EGRIP drill site at the onset region of the Northeast Greenland Ice Stream, https://doi.org/10.1594/PANGAEA.914258, 2020.

605   Johnsen, S. J., Clausen, H. B., Dansgaard, W., Fuhrer, K., Gundestrup, N., Hammer, C. U., Iversen, P., Jouzel, J., Stauffer, B., and Steffensen, J. P.: Irregular glacial interstadials recorded in a new Greenland ice core, Nature, 359, 311–313, https://doi.org/10.1038/359311a0, 1992.

Johnsen, S. J., Dahl-Jensen, D., Dansgaard, W., and Gundestrup, N.: Greenland palaeotemperatures derived from GRIP bore hole temperature and ice core isotope profiles, Tellus, Series B, 47 B, 624–629, https://doi.org/10.3402/tellusb.v47i5.16077, 1995.

Joughin, I., Fahnestock, M., MacAyeal, D., Bamber, J. L., and Gogineni, P.: Observation and analysis of ice flow in the largest Greenland ice
610   stream, Journal of Geophysical Research: Atmospheres, 106, 34 021–34 034, https://doi.org/10.1029/2001JD900087, 2001.

Joughin, I., Smith, B. E., and Howat, I. M.: A complete map of Greenland ice velocity derived from satellite data collected over 20 years, Journal of Glaciology, 64, 1–11, https://doi.org/10.1017/jog.2017.73, 2018.

Jouzel, J., Alley, R. B., Cuffey, K. M., Dansgaard, W., Grootes, P., Hoffmann, G., Johnsen, S. J., Koster, R. D., Peel, D., Shuman, C. A., Stievenard, M., Stuiver, M., and White, J.: Validity of the temperature reconstruction from water isotopes in ice cores, Journal of Geo-
615   physical Research: Oceans, 102, 26 471–26 487, https://doi.org/10.1029/97JC01283, 1997.

Keisling, B. A., Christianson, K., Alley, R. B., Peters, L. E., Christian, J. E., Anandakrishnan, S., Riverman, K. L., Muto, A., and Jacobel, R. W.: Basal conditions and ice dynamics inferred from radar-derived internal stratigraphy of the northeast Greenland ice stream, Annals of Glaciology, 55, 127–137, https://doi.org/10.3189/2014AoG67A090, 2014.

Khan, S. A., Kjær, K. H., Bevis, M., Bamber, J. L., Wahr, J., Kjeldsen, K. K., Bjørk, A. A., Korsgaard, N. J., Stearns, L. A., Van Den Broeke, M. R., Liu, L., Larsen, N. K., and Muresan, I. S.: Sustained mass loss of the northeast Greenland ice sheet triggered by regional warming, Nature Climate Change, 4, 292–299, https://doi.org/10.1038/nclimate2161, 2014.

Koutnik, M. R., Fudge, T., Conway, H., Waddington, E. D., Neumann, T. A., Cuffey, K. M., Buizert, C., and Taylor, K. C.: Holocene accumulation and ice flow near the West Antarctic Ice Sheet Divide ice core site, Journal of Geophysical Research: Earth Surface, 121, 907–924, https://doi.org/10.1002/2015JF003668, 2016.

Lawver, L. A. and Müller, R. D.: Iceland hotspot track, Geology, 22, 311–314, 1994.

Letréguilly, A., Reeh, N., and Huybrechts, P.: The Greenland ice sheet through the last glacial-interglacial cycle, Palaeogeography, Palaeoclimatology, Palaeoecology, 90, 385–394, https://doi.org/https://doi.org/10.1016/S0031-0182(12)80037-X, 1991.

Leysinger Vieli, G. J., Martín, C., Hindmarsh, R. C., and Lüthi, M. P.: Basal freeze-on generates complex ice-sheet stratigraphy, Nature Communications, 9, 1–13, https://doi.org/10.1038/s41467-018-07083-3, 2018.

Lorius, C., Jouzel, J., Ritz, C., Merlivat, L., Barkov, N. I., Korotkevich, Y. S., and Kotlyakov, V. M.: A 150,000-year climatic record from Antarctic ice, Nature, 316, 591–596, https://doi.org/10.1038/316591a0, 1985.

MacGregor, J. A., Fahnestock, M. A., Catania, G. A., Paden, J. D., Prasad Gogineni, S., Young, S. K., Rybarski, S. C., Mabrey, A. N., Wagman, B. M., and Morlighem, M.: Radiostratigraphy and age structure of the Greenland Ice Sheet, Journal of Geophysical Research: Earth Surface, 120, 212–241, https://doi.org/10.1002/2014JF003215, 2015.

MacGregor, J. A., Fahnestock, M. A., Catania, G. A., Aschwanden, A., Clow, G. D., Colgan, W. T., Gogineni, S. P., Morlighem, M., Nowicki, S. M., Paden, J. D., Price, S. F., and Seroussi, H.: A synthesis of the basal thermal state of the Greenland Ice Sheet, Journal of Geophysical Research: Earth Surface, 121, 1328–1350, https://doi.org/10.1002/2015JF003803, 2016.

Marcott, S. A., Bauska, T. K., Buizert, C., Steig, E. J., Rosen, J. L., Cuffey, K. M., Fudge, T. J., Severinghaus, J. P., Ahn, J., Kalk, M. L., McConnell, J. R., Sowers, T., Taylor, K. C., White, J. W., and Brook, E. J.: Centennial-scale changes in the global carbon cycle during the last deglaciation, Nature, 514, 616–619, https://doi.org/10.1038/nature13799, 2014.

Marshall, S. J. and Cuffey, K. M.: Peregrinations of the Greenland Ice Sheet divide in the last glacial cycle: Implications for central Greenland ice cores, Earth and Planetary Science Letters, 179, 73–90, https://doi.org/10.1016/S0012-821X(00)00108-4, 2000.

Meese, D. A., Gow, A. J., Alley, R. B., Zielinski, G. A., Grootes, P. M., Ram, M., Taylor, K. C., Mayewski, P. A., and Bolzan, J. F.: The Greenland Ice Sheet Project 2 depth-age scale: Methods and results, Journal of Geophysical Research: Oceans, 102, 26 411–26 423, https://doi.org/10.1029/97JC00269, 1997.

Metropolis, N., Rosenbluth, A. W., Rosenbluth, M. N., Teller, A. H., and Teller, E.: Equation of state calculations by fast computing machines, The Journal of Chemical Physics, 21, 1087–1092, https://doi.org/10.1063/1.1699114, 1953.

Millar, D.: Acidity levels in ice sheets from radio echo-sounding, Annals of Glaciology, 3, 199–203, 1982.

Mojtabavi, S., Wilhelms, F., Cook, E., Davies, S., Sinnl, G., Skov Jensen, M., Dahl-Jensen, D., Svensson, A., Vinther, B., Kipfstuhl, S., Jones, G., Karlsson, N., Faria, S. H., Gkinis, V., Kjær, H., Erhardt, T., Berben, S., Nisancioglu, K., Koldtoft, I., and Rasmussen, S. O.: A first chronology for the East GReenland Ice-core Project (EGRIP) over the Holocene and last glacial termination, Climate of the Past, 16, 2359–2380, https://doi.org/10.5194/cp-2019-143, 2020.

Morlighem, M., Williams, C. N., Rignot, E., An, L., Arndt, J. E., Bamber, J. L., Catania, G., Chauché, N., Dowdeswell, J. A., Dorschel, B., Fenty, I., Hogan, K., Howat, I., Hubbard, A., Jakobsson, M., Jordan, T. M., Kjeldsen, K. K., Millan, R., Mayer, L., Mouginot, J., Noël, B. P., O'Cofaigh, C., Palmer, S., Rysgaard, S., Seroussi, H., Siegert, M. J., Slabon, P., Straneo, F., van den Broeke, M. R., Weinrebe, W., Wood, M., and Zinglersen, K. B.: BedMachine v3: Complete Bed Topography and Ocean Bathymetry Mapping of Greenland From Multibeam Echo Sounding Combined With Mass Conservation, Geophysical Research Letters, 44, 11,051–11,061, https://doi.org/10.1002/2017GL074954, 2017.

Mosegaard, K. and Tarantola, A.: Monte Carlo sampling of solutions to inverse problems, Journal of Geophysical Research, 100, 12 431 –12 447, https://doi.org/10.1029/94jb03097, 1995.

Mottram, R., Simonsen, S. B., Svendsen, S. H., Barletta, V. R., Sørensen, L. S., Nagler, T., Wuite, J., Groh, A., Horwath, M., Rosier, J., Solgaard, A., Hvidberg, C. S., and Forsberg, R.: An integrated view of greenland ice sheet mass changes based on models and satellite observations, Remote Sensing, 11, 1–26, https://doi.org/10.3390/rs11121407, 2019.

NEEM Community members, Dahl-Jensen, D., Albert, M., Aldahan, A., Azuma, N., Balslev-Clausen, D., Baumgartner, M., Berggren, A.-M., Bigler, M., Binder, T., Blunier, T., Bourgeois, J. C., Brook, E. J., Chuchardt, S. L., Buizert, C., Capron, E., Chappellaz, J., Chung, J., Clausen, H. B., Cvijanovic, I., Davis, S. M., Ditlevsen, P., Eicher, O., Fischer, H., Fisher, D. A., Fleet, L., Gfeller, G., Gkinis, V., Gogineni, S., Goto-Azuma, K., Grinsted, A., Gudlaugsdottir, H., Guillevic, M., Hansen, S. B., Hansson, M., Hirabayashi, M., Hong, S., Hur, S. D., Huybrechts, P., Hvidberg, C., Iizuka, Y., Jenk, T., Johnsen, S. J., Jones, T. R., Jouzel, J., Karlsson, N. B., Kawamura, K., Keegan, K., Kettner, E., Kipfstuhl, S., Kjær, H. A., Koutnik, M., Kuramoto, T., Köhler, P., Laepple, T., Landais, A., Langen, P., Larsen, L. B., Leuenberger, D., Leuenberger, M., Leuschen, C., Li, J., Lippenkov, V., Mirtinerie, P., Maselli, O. J., Masson-Delmotte, V., McConnel, J. R., Miller, H., Mini, O., Miyamoto, A., Montagnat-Rentier, M., Mulvaney, R., Muscheler, R., Orsi, A. J., Paden, J., Panton, C., Pattyn, F., Petit, J. R., Pol, K., Popp, T., Possnert, G., Prié, F., Prokopiou, M., Quique, A., Rasmussen, S. O., Raynaud, D., Ren, J., Reutenauer, C., Ritz, C., Roeckeman, T., Rosen, J. L., Rubino, M., Rybak, O., Samyn, D., Sapart, C. J., Schilt, A., Schmidt, A., Schwander, J., Schüpbach, S., Seierstad, I., Severinghaus, J. P., Sheldon, S., Simonsen, S. B., Sjolte, J., Solgaard, A. M., Sowers, T., Sperlich, P., Steen-Larsen, H. C., Steffen, K., Steffensen, J. P., Steinhage, D., Stocker, T., Stowasser, C., Sturevik, A. S., Sturges, B., Sveinbjörnsdottir, A., Svensson, A., Tison, J.-L., Uetake, J., Vallelonga, P., van de Wal, R. S. W., van der Wel, G., Vaughn, B. H., Vinther, B., Waddington, E., Wegner, A., Weikusat, I., White, J. W. C., Wilhelms, F., Winstrup, M., Witrant, E., Wolff, E., Xiao, C., and Zheng, J.: Eemian interglacial reconstructed from a Greenland folded ice core, Nature, 493, 489–494, https://doi.org/10.1038/nature11789, 2013.

Paren, J. G. and Robin, G. d. Q.: Internal Reflections in Polar Ice Sheets, Journal of Glaciology, 14, 251–259, https://doi.org/10.3189/s0022143000021730, 1975.

Parrenin, F., Barnola, J. M., Beer, J., Blunier, T., Castellano, E., Chappellaz, J., Dreyfus, G., Fischer, H., Fujita, S., Jouzel, J., Kawamura, K., Lemieux-Dudon, B., Loulergue, L., Masson-Delmotte, V., Narcisi, B., Petit, J. R., Raisbeck, G., Raynaud, D., Ruth, U., Schwander, J., Severi, M., Spahni, R., Steffensen, J. P., Svensson, A., Udisti, R., Waelbroeck, C., and Wolff, E.: The EDC3 chronology for the EPICA Dome C ice core, Climate of the Past, 3, 485–497, https://doi.org/10.5194/cp-3-485-2007, 2007.

Petit, J. R., Raynaud, D., Basile, I., Chappellaz, J., Davisk, M., Ritz, C., Delmotte, M., Legrand, M., Lorius, C., Pe, L., and Saltz-mank, E.: Climate and atmospheric history of the past 420,000 years from the Vostok ice core , Antarctica, Nature, 399, 429–436, https://doi.org/10.1038/20859, 1999.

Porter, C., Morin, P., Howat, I., Noh, M.-J., Bates, B., Peterman, K., Keesey, S., Schlenk, M., Gardiner, J., Tomko, K., Willis, M., Kelleher, C., Cloutier, M., Husby, E., Foga, S., Nakamura, H., Platson, M., Wethington, Michael, J., Williamson, C., Bauer, G.,

690   Enos, J., Arnold, G., Kramer, W., Becker, P., Doshi, A., D'Souza, C., Cummens, P., Laurier, F., and Bojesen, M.: ArcticDEM,
       https://doi.org/10.7910/DVN/OHHUKH, 2018.

       Raisbeck, G. M., Yiou, F., Jouzel, J., and Stocker, T. F.: Direct north-south synchronization of abrupt climate change record in ice cores using
       Beryllium 10, Climate of the Past, 3, 541–547, https://doi.org/10.5194/cp-3-541-2007, 2007.

       Rasmussen, S. O., Andersen, K. K., Svensson, A. M., Steffensen, J. P., Vinther, B. M., Clausen, H. B., Siggaard-Andersen, M. L.,
695   Johnsen, S. J., Larsen, L. B., Dahl-Jensen, D., Bigler, M., Röthlisberger, R., Fischer, H., Goto-Azuma, K., Hansson, M. E., and Ruth,
       U.: A new Greenland ice core chronology for the last glacial termination, Journal of Geophysical Research: Atmospheres, 111, 1–16,
       https://doi.org/10.1029/2005JD006079, 2006.

       Rasmussen, S. O., Abbott, P. M., Blunier, T., Bourne, A. J., Brook, E., Buchardt, S. L., Buizert, C., Chappellaz, J., Clausen, H. B., Cook, E.,
       Dahl-Jensen, D., Davies, S. M., Guillevic, M., Kipfstuhl, S., Laepple, T., Seierstad, I. K., Severinghaus, J. P., Steffensen, J. P., Stowasser,
700   C., Svensson, A., Vallelonga, P., Vinther, B. M., Wilhelms, F., and Winstrup, M.: A first chronology for the north greenland eemian ice
       drilling (NEEM) ice core, Climate of the Past, 9, 2713–2730, https://doi.org/10.5194/cp-9-2713-2013, 2013.

       Rasmussen, S. O., Bigler, M., Blockley, S. P., Blunier, T., Buchardt, S. L., Clausen, H. B., Cvijanovic, I., Dahl-Jensen, D., Johnsen, S. J.,
       Fischer, H., et al.: A stratigraphic framework for abrupt climatic changes during the Last Glacial period based on three synchronized
       Greenland ice-core records: refining and extending the INTIMATE event stratigraphy, Quaternary Science Reviews, 106, 14–28, 2014.

705   Raynaud, D., Chappellaz, J., Ritz, C., and Martinerie, P.: Air content along the Greenland Ice Core Project core: A record of
       surface climatic parameters and elevation in central Greenland, Journal of Geophysical Research: Oceans, 102, 26 607–26 613,
       https://doi.org/10.1029/97JC01908, 1997.

       Rignot, E. and Mouginot, J.: Ice flow in Greenland for the international polar year 2008–2009, Geophysical Research Letters, 39, 1–7,
       https://doi.org/10.1029/2012GL051634, 2012.

710   Riverman, K. L., Alley, R. B., Anandakrishnan, S., Christianson, K., Holschuh, N. D., Medley, B., Muto, A., and Peters, L. E.: Enhanced Firn
       Densification in High-Accumulation Shear Margins of the NE Greenland Ice Stream, Journal of Geophysical Research: Earth Surface,
       124, 365–382, https://doi.org/10.1029/2017JF004604, 2019.

       Robel, A. A., Degiuli, E., Schoof, C., and Tziperman, E.: Dynamics of ice stream temporal variability: Modes, scales, and hysteresis, Journal
       of Geophysical Research: Earth Surface, 118, 925–936, https://doi.org/10.1002/jgrf.20072, 2013.

715   Robin, G. d. Q. and Millar, D. H. M.: Flow Of Ice Sheets In The Vicinity Of Subglacial Peaks, Annals of Glaciology, 3, 290–294,
       https://doi.org/10.3189/s0260305500002949, 1982.

       Robin, G. d. Q., Evans, S., and Bailey, J. T.: Interpretation of radio echo sounding in polar ice sheets, Philosophical Transactions of the Royal
       Society of London. Series A, Mathematical and Physical Sciences, 265, 437–505, 1969.

       Salamatin, A. N., Lipenkov, V. Y., Barkov, N. I., Jouzel, J., Petit, J. R., and Raynaud, D.: Ice core age dating and paleothermometer calibration
720   based on isotope and temperature profiles from deep boreholes at Vostok Station (East Antarctica), Journal of Geophysical Research:
       Atmospheres, 103, 8963–8977, https://doi.org/10.1029/97JD02253, 1998.

       Seierstad, I. K., Abbott, P. M., Bigler, M., Blunier, T., Bourne, A. J., Brook, E., Buchardt, S. L., Buizert, C., Clausen, H. B., Cook, E.,
       Dahl-Jensen, D., Davies, S. M., Guillevic, M., Johnsen, S. J., Pedersen, D. S., Popp, T. J., Rasmussen, S. O., Severinghaus, J. P.,
       Svensson, A., and Vinther, B. M.: Consistently dated records from the Greenland GRIP, GISP2 and NGRIP ice cores for the past
725   104ka reveal regional millennial-scale δ18O gradients with possible Heinrich event imprint, Quaternary Science Reviews, 106, 29–46,
       https://doi.org/10.1016/j.quascirev.2014.10.032, 2014.

Shepherd, A., Ivins, E., Rignot, E., Smith, B., van den Broeke, M., Velicogna, I., Whitehouse, P., Briggs, K., Joughin, I., Krinner, G., Nowicki, S., Payne, T., Scambos, T., Schlegel, N., A, G., Agosta, C., Ahlstrøm, A., Babonis, G., Barletta, V. R., Bjørk, A. A., Blazquez, A., Bonin, J., Colgan, W., Csatho, B., Cullather, R., Engdahl, M. E., Felikson, D., Fettweis, X., Forsberg, R., Hogg, A. E., Gallee, H., Gardner, A.,

730 Gilbert, L., Gourmelen, N., Groh, A., Gunter, B., Hanna, E., Harig, C., Helm, V., Horvath, A., Horwath, M., Khan, S., Kjeldsen, K. K., Konrad, H., Langen, P. L., Lecavalier, B., Loomis, B., Luthcke, S., McMillan, M., Melini, D., Mernild, S., Mohajerani, Y., Moore, P., Mottram, R., Mouginot, J., Moyano, G., Muir, A., Nagler, T., Nield, G., Nilsson, J., Noël, B., Otosaka, I., Pattle, M. E., Peltier, W. R., Pie, N., Rietbroek, R., Rott, H., Sandberg Sørensen, L., Sasgen, I., Save, H., Scheuchl, B., Schrama, E., Schröder, L., Seo, K. W., Simonsen, S. B., Slater, T., Spada, G., Sutterley, T., Talpe, M., Tarasov, L., van de Berg, W. J., van der Wal, W., van Wessem, M., Vishwakarma,

735 B. D., Wiese, D., Wilton, D., Wagner, T., Wouters, B., and Wuite, J.: Mass balance of the Greenland Ice Sheet from 1992 to 2018, Nature, 579, 233–239, https://doi.org/10.1038/s41586-019-1855-2, 2020.

Siegert, M.: On the origin, nature and uses of Antarctic ice-sheet radio-echo layering, Progress in Physical Geography, 23, 159–179, https://doi.org/10.1191/030913399671124903, 1999.

Simonsen, S. B. and Sørensen, L. S.: Implications of changing scattering properties on Greenland ice sheet volume change from Cryosat-2

740 altimetry, Remote Sensing of Environment, 190, 207–216, https://doi.org/10.1016/j.rse.2016.12.012, 2017.

Smith-Johnsen, S., Schlegel, N. J., de Fleurian, B., and Nisancioglu, K. H.: Sensitivity of the Northeast Greenland Ice Stream to Geothermal Heat, Journal of Geophysical Research: Earth Surface, 125, 1–14, https://doi.org/10.1029/2019JF005252, 2020.

Svensson, A., Andersen, K. K., Bigler, M., Clausen, H. B., Dahl-Jensen, D., Davies, S. M., Johnsen, S. J., Muscheler, R., Parrenin, F., Rasmussen, S. O., Röthlisberger, R., Seierstad, I., Steffensen, J. P., and Vinther, B. M.: A 60 000 year Greenland stratigraphic ice core

745 chronology, Climate of the Past, 4, 47–57, https://doi.org/10.5194/cp-4-47-2008, 2008.

Tulaczyk, S., Kamb, W. B., and Engelhardt, H. F.: Basal mechanics of Ice Stream B, West Antarctica: 1. Till mechanics, Journal of Geophysical Research: Solid Earth, 105, 463–481, https://doi.org/10.1029/1999jb900329, 2000.

Vallelonga, P., Christianson, K., Alley, R., Anandakrishnan, S., Christian, J., Dahl-Jensen, D., Gkinis, V., Holme, C., Jacobel, R., Karlsson, N., et al.: Initial results from geophysical surveys and shallow coring of the Northeast Greenland Ice Stream (NEGIS), The Cryosphere,

750 8, 1275–1287, https://doi.org/10.5194/tc-8-1275-2014, 2014.

Vinther, B., Buchardt, S., Clausen, H., Dahl-Jensen, D., Johnsen, S., Fisher, D., Koerner, R., Raynaud, D., Lipenkov, V., Andersen, K. K., et al.: Holocene thinning of the Greenland ice sheet, Nature, 461, 385–388, https://doi.org/10.1038/nature08355, 2009.

Waddington, E. D., Neumann, T. A., Koutnik, M. R., Marshall, H. P., and Morse, D. L.: Inference of accumulation-rate patterns from deep layers in glaciers and ice sheets, Journal of Glaciology, 53, 694–712, https://doi.org/10.3189/002214307784409351, 2007.

755 Walker, M., Johnes, S., Rasmussen, S. O., Popp, T., Steffensen, J.-P., Gibbard, P., Hoek, W., Lowe, J., Andrews, J., Björck, S., Cwynar, L. C., Hughen, K., Kershaw, P., Kromer, B., Litt, T., Lowe, D. J., Nakagawa, T., Newnham, R., and Schwander, J.: Formal definition and dating of the GSSP (Global Stratotype Section and Point) for the base of the Holocene using the Greenland NGRIP ice core, and selected auxiliary records, Journal of Quaternary Science, 24, 3–17, https://doi.org/10.1002/jqs, 2009.

Weertman, J.: Sliding–no sliding zone effect and age determination of ice cores, Quaternary Research, 6, 203–207,

760 https://doi.org/10.1016/0033-5894(76)90050-8, 1976.

Whillans, I. M.: Radio-echo layers and the recent stability of the West Antarctic ice sheet, Nature, 264, 152–155, https://doi.org/10.1038/264152a0, 1976.

Whillans, I. M. and Johnsen, S. J.: Longitudinal variations in glacial flow: theory and test using data from the Byrd Station strain network, Antarctica., Journal of Glaciology, 29, 78–97, https://doi.org/10.1017/S0022143000005165, 1983.

765 Wolovick, M. J., Creyts, T. T., Buck, W. R., and Bell, R. E.: Traveling slippery patches produce thickness-scale folds in ice sheets, Geophysical Research Letters, 41, 8895–8901, https://doi.org/10.1002/2014GL062248, 2014.

Yiou, F., Raisbeck, G. M., Baumgartner, S., Beer, J., Hammer, C., Johnsen, S., Jouzel, J., Kubik, P. W., Lestringuez, J., Stiévenard, M., Suter, M., and Yiou, P.: Beryllium 10 in the Greenland Ice Core Project ice core at Summit, Greenland, Journal of Geophysical Research: Oceans, 102, 26 783–26 794, https://doi.org/10.1029/97JC01265, 1997.

770 Zeising, O. and Humbert, A.: Indication of high basal melting at EastGRIP drill site on the Northeast Greenland Ice Stream, The Cryosphere Discussions, pp. 1–15, https://doi.org/10.5194/tc-2021-37, in review, 2021.